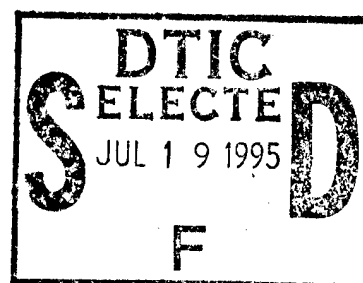


PL-TR-94-2216

RADIATIVE CHARACTERISTICS OF CLOUDS MEASURED FROM SATELLITES

Donald P. Wylie

University of Wisconsin
Space Science & Engineering Center
1225 W. Dayton Street
Madison, WI 53706



22 December 1994

Scientific Report No. 1

Approved for public release; distribution unlimited

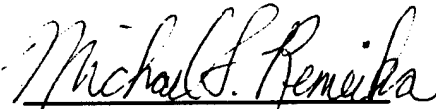


PHILLIPS LABORATORY
Directorate of Geophysics
AIR FORCE MATERIEL COMMAND
HANSCOM AFB, MA 01731-3010

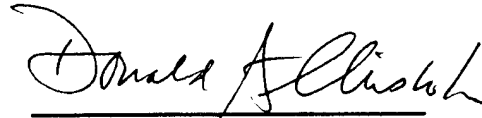
19950717 066

DTIC QUALITY INSPECTED 4

"This technical report has been reviewed and is approved for publication."



MICHAEL F. REMEIKA
Contract Manager



DONALD A. CHISHOLM
Chief, Satellite Analysis and Weather
Prediction Branch
Atmospheric Sciences Division



ROBERT A. McCLATCHEY, Director
Atmospheric Sciences Division

This report has been reviewed by the ESC Public Affairs Office (PA) and is releasable to the National Technical Information Service (NTIS).

Qualified requestors may obtain additional copies from the Defense Technical Information Center (DTIC). All others should apply to the National Technical Information Service (NTIS).

If your address has changed, or if you wish to be removed from the mailing list, or if the addressee is no longer employed by your organization, please notify PL/IM, 29 Randolph Road, Hanscom AFB, MA 01731-3010. This will assist us in maintaining a current mailing list.

Do not return copies of this report unless contractual obligations or notices on a specific document requires that it be returned.

REPORT DOCUMENTATION PAGE			Form Approved OMB No. 0704-0188	
Public reporting burden for this collection of information is estimated to average 1 hour per response, including the time for reviewing instructions, searching existing data sources, gathering and maintaining the data needed, and completing and reviewing the collection of information. Send comments regarding this burden estimate or any other aspect of this collection of information, including suggestions for reducing this burden, to Washington Headquarters Services, Directorate for Information Operations and Reports, 1215 Jefferson Davis Highway, Suite 1204, Arlington, VA 22202-4302, and to the Office of Management and Budget, Paperwork Reduction Project (0704-0188), Washington, DC 20503.				
1. AGENCY USE ONLY (Leave blank)	2. REPORT DATE Dec. 22, 1994	3. REPORT TYPE AND DATES COVERED Scientific No. 1		
4. TITLE AND SUBTITLE Radiative Characteristics of Clouds Measured from Satellites		5. FUNDING NUMBERS F19628-91-K-0007 PE62101F PR6670 TA17 WU BC		
6. AUTHOR(S) Donald Wylie				
7. PERFORMING ORGANIZATION NAME(S) AND ADDRESS(ES) Space Science and Engineering Center University of Wisconsin-Madison 1225 W. Dayton Street Madison, WI 53706		8. PERFORMING ORGANIZATION REPORT NUMBER		
9. SPONSORING/MONITORING AGENCY NAME(S) AND ADDRESS(ES) Phillips Laboratory 29 Randolph Road Hanscom AFB, MA 01731-3010 Contract Manager Major Michael F. Remeika/GPAB		10. SPONSORING/MONITORING AGENCY REPORT NUMBER PL-TR-94-2216		
11. SUPPLEMENTARY NOTES				
12a. DISTRIBUTION/AVAILABILITY STATEMENT Approved for public release; distribution			12b. DISTRIBUTION CODE	
13. ABSTRACT (Maximum 200 words) The significant findings reported in this paper are: 1) Cirrus clouds are very common and were found in 42% of the satellite data. There are seasonal changes in the locations of the most frequent cirrus which follow seasonal changes in convective clouds. However, very thin cirrus occurred at least 10% of the time in all areas. The diurnal cycle of cirrus was very small over the oceans. The diurnal cycle over land followed the diurnal cycle of convective clouds. 2) A large increase in cirrus and high cloud frequency was found in 1991. This cloud cover increase appeared with the strong El Nino - Southern Oscillation climate event. A volcanic eruption also occurred in 1991 which may have enhanced this cloud cover change. It should be noted that the total cloud cover of all cloud forms did not change during this period.				
14. SUBJECT TERMS Clouds, cloud cover statistics, cirrus, global cloud cover, satellite cloud statistics			15. NUMBER OF PAGES 60	
			16. PRICE CODE	
17. SECURITY CLASSIFICATION OF REPORT UNCLASSIFIED	18. SECURITY CLASSIFICATION OF THIS PAGE UNCLASSIFIED	19. SECURITY CLASSIFICATION OF ABSTRACT UNCLASSIFIED	20. LIMITATION OF ABSTRACT SAR	

CONTENTS

INTRODUCTION	1
Appendix A: Four Years of Global Cirrus Cloud Statistics Using HIRS	3
Appendix B: Understanding Satellite Cirrus Cloud Climatologies With Calibrated Lidar Optical Depths	19

Accession For	
NTIS CRA&I	<input checked="checked" type="checkbox"/>
DTIC TAB	<input type="checkbox"/>
Unannounced	<input type="checkbox"/>
Justification	
By	
Distribution /	
Availability Codes	
Dist	Avail and/or Special
A-1	

Introduction

Data collection has continued from both the polar orbiting NOAA satellites and the geostationary GOES satellite. The collection of these data and cloud analyses are done automatically on the McIDAS at the University of Wisconsin-Madison. Two analyses of these data have been completed in the last year which will be discussed in this report.

A paper summarizing the global cloud statistics entitled "Four Years of Global Cirrus Cloud Statistics Using HIRS" has been published in the December, 1994, issue of the Journal of Climate. A copy is enclosed as Appendix A. The data collected and method of analysis are also discussed in that paper. The significant findings reported in this paper are:

a. Cirrus clouds are very common and were found in 42% of the satellite data. There are seasonal changes in the locations of the most frequent cirrus which follow seasonal changes in convective clouds. However, very thin cirrus occurred at least 10% of the time in all areas. The diurnal cycle of cirrus was very small over the oceans. The diurnal cycle of cirrus over land was found to follow the diurnal cycle of convective clouds in a previous study using the GOES data.

b. A large increase in cirrus and high cloud cover was found in 1991. This cloud cover increase appeared with the strong El Nino Southern Oscillation climatic event. A volcanic eruption also occurred in 1991 which may have enhanced this cloud cover change. It should be noted that the total cloud cover of all cloud forms did not change during this period. Cloud free observations continued to be 23% of the data before and after the high cloud change.

Summaries of these cloud data have been given to Al Boehm of STC and to Ian Robinson and Donald Rudy of the Aerospace Corporation for their studies of cloud cover. Their analyses of these data were published in Aerospace Report No. ATR-94(8019-1), "Frequency of Cloud Cover at Altitude: Implications for Surveillance Systems" by Robinson, Rudy and Gonzalez.

A comparison of our cloud data is also being made to two other satellite cloud climatologies with similar and complementary information. The International Satellite Cloud Climatology Project (ISCCP) has compared their cloud statistics to ours. A paper is being drafted by a NASA group on this comparison. The conclusions will be that we find similar geographical distributions of cirrus along with similar seasonal changes. However, the frequency of cirrus and other cloud forms are less in the ISCCP analysis than ours.

A comparison with the Stratospheric Aerosol and Gas Experiment (SAGE) cloud data is being made. The first results show similar frequencies of high clouds in both data sets.

We have compared our satellite data to lidar observations of clouds. A paper describing the first results of this comparison is included in Appendix B. It shows that the optical depth calculations from satellite infrared data agree with similar optical depths measured in visible wavelengths by the lidar. This study also found the cloud height calculated from the CO2 Slicing Algorithm represents the denser part of semi-transparent cirrus clouds rather than the height of the cloud top. This cloud level is more useful for radiative transfer calculations than the cloud top height.

Appendix A

Reprinted from JOURNAL OF CLIMATE, Vol. 7, No. 12, December 1994
American Meteorological Society

Four Years of Global Cirrus Cloud Statistics Using HIRS

DONALD P. WYLIE

W. PAUL MENZEL AND HAROLD M. WOOLF

KATHLEEN I. STRABALA

The U.S. Government is authorized to reproduce and sell this report.
Permission for further reproduction by others must be obtained from
the copyright owner.

Four Years of Global Cirrus Cloud Statistics Using HIRS

DONALD P. WYLIE

Space Science and Engineering Center, University of Wisconsin-Madison, Madison, Wisconsin

W. PAUL MENZEL AND HAROLD M. WOOLF

Satellite Applications Laboratory, NOAA/NESDIS, Madison, Wisconsin

KATHLEEN I. STRABALA

Space Science and Engineering Center, University of Wisconsin-Madison, Madison, Wisconsin

(Manuscript received 2 July 1993, in final form 3 February 1994)

ABSTRACT

Trends in global upper-tropospheric transmissive cirrus cloud cover are beginning to emerge from a four-year cloud climatology using NOAA polar-orbiting High-Resolution Infrared Radiation Sounder (HIRS) multispectral data. Cloud occurrence, height, and effective emissivity are determined with the CO₂ slicing technique on the four years of data (June 1989–May 1993). There is a global preponderance of transmissive high clouds, 42% on the average; about three-fourths of these are above 500 hPa and presumed to be cirrus. In the ITCZ, a high frequency of cirrus (greater than 50%) is found at all times; a modest seasonal movement tracks the sun. Large seasonal changes in cloud cover occur over the oceans in the storm belts at midlatitudes; the concentrations of these clouds migrate north and south with the seasons following the progressions of the subtropical highs (anticyclones). More cirrus is found in the summer than in the winter in each hemisphere.

A significant change in cirrus cloud cover occurs in 1991, the third year of the study. Cirrus observations increase from 35% to 43% of the data, a change of eight percentage points. Other cloud forms, opaque to terrestrial radiation, decrease by nearly the same amount. Most of the increase is thinner cirrus with infrared optical depths below 0.7. The increase in cirrus happens at the same time as the 1991–92 El Niño/Southern Oscillation (ENSO) and the eruption of Mt. Pinatubo. The cirrus changes occur at the start of the ENSO and persist into 1993 in contrast to other climatic indicators that return to near pre-ENSO and volcanic levels in 1993.

1. Introduction

Cirrus clouds are crucially important to global radiative processes and the thermal balance of the earth; they allow solar heating while reducing infrared radiation cooling to space. Models of climate changes must correctly simulate these clouds to properly account for radiometric effects in the earth's energy budget. Past estimates of the variation of cloud cover and the earth's outgoing longwave radiation have been derived primarily from longwave infrared window (10–12 μm) radiances observed from polar-orbiting and geostationary satellites (Rossow and Lacis 1990; Gruber and Chen 1988; Stowe et al. 1988). The occurrence of transmissive clouds has been underestimated in these single-band approaches. Recently, multispectral techniques have been used to better detect cirrus clouds in global (Wu and Susskind 1990) and North American

(Wylie and Menzel 1989; Menzel et al. 1992) cloud studies.

This paper reports on the investigation of seasonal changes in semitransparent or cirrus global cloud cover with multispectral observations from polar orbiting HIRS (High-Resolution Infrared Radiation Sounder). Clouds partially transparent to terrestrial radiation are separated from opaque clouds in four-year statistics of cloud cover (Wylie and Menzel 1989). Transmissive or cirrus clouds are found in roughly 40% of all satellite observations.

The HIRS observations in the carbon dioxide absorption band at 15 μm are used to calculate these cloud statistics. The CO₂ slicing algorithm calculates both cloud-top pressure and effective emissivity from radiative transfer principles. Various CO₂ algorithms have been described in the literature (Chahine 1974; Smith et al. 1974; McCleese and Wilson 1976; Smith and Platt 1978; Wielicki and Coakley 1981; Menzel et al. 1983) and applications to data from the geostationary sounder VAS [VISSR (Visible and Infrared Spin Scan Radiometer) Atmospheric Sounder] and the po-

Corresponding author address: D. P. Wylie, Space Science and Engineering Center, University of Wisconsin-Madison, 1225 West Dayton Street, Madison, WI 53706.

lar orbiting sounder HIRS have been published (Wylie and Menzel 1989; Menzel et al. 1986; Susskind et al. 1987; Menzel et al. 1989; Eyre and Menzel 1989).

2. Technique

Cirrus clouds often appear warmer in the infrared window band than the ambient air temperature at their altitude because they are transmitting radiation from below. This occurs in more than 40% of the satellite data, of which roughly half is often misinterpreted as lower noncirrus clouds. The CO₂ slicing technique is capable of correctly identifying most of these clouds. Using the HIRS infrared bands with partial CO₂ absorption, cloud-top pressure and effective emissivity are calculated for each observational area. Carbon dioxide slicing does not estimate cloud-base pressure. Partially transmissive clouds are distinguished during daylight and night over water and land. The description of the technique and details of its application with HIRS data are presented in Menzel et al. (1986) and Menzel et al. (1989) and are repeated in appendix A of this paper; there are similarities to the application with VAS data described in Wylie and Menzel (1989).

Effective emissivity refers to the product of the fractional cloud cover N and the cloud emissivity ϵ for each observational area (roughly 20 km \times 20 km). When $N\epsilon$ is less than unity, HIRS may be observing broken cloud ($N < 1$, $\epsilon = 1$), overcast transmissive cloud ($N = 1$, $\epsilon < 1$), or broken transmissive cloud ($N < 1$, $\epsilon < 1$). All of these possibilities imply an observation where the HIRS radiometer detects radiation from below a cloud layer as well as radiation from the cloud-layer top. All observations where the effective emissivity is less than 0.95 are labeled as "cirrus" in this paper. Effective emissivity observations greater than 0.95 are considered to be opaque clouds.

Cirrus usually are transmissive and exhibit spatial variations at scales ranging from hundreds of kilometers to smaller than the field of view (FOV) of the instrument. The assumption is that more of the semi-transparency for a given field of view is due to cloud emissivity being less than 1 than due to the cloud not completely covering the field of view. Comparison of Advanced Very High Resolution Radiometer (AVHRR) 1-km resolution cloud data and HIRS 20-km resolution cloud effective emissivity determinations supports this. For effective emissivity determinations greater than 0.50, almost all of the variation from one FOV to another is caused by changes in emissivity and not cloud fraction. For effective emissivities less than 0.50, most of the variation is still being caused by changes in cloud emissivity fraction, but some is now being caused by changes in cloud fraction. Appendix B presents this comparison. Thus, for most synoptic regimes, especially in the Tropics and subtropics, this assumption appears reasonable and is supported in the literature (Wielicki and Parker 1992; Baum et al. 1992).

In multiple cloud layers, the technique is limited to finding the height of only the highest cloud layer. Multiple layers often can be inferred from inspection of neighboring pixels where holes in the upper layer occur. Comparison to cloud reports from ground observers indicates that 50% of the time when the CO₂ technique detects an upper-tropospheric cloud, one or more lower cloud layers also is present (Menzel and Strabala 1989). When an opaque cloud underlies a transmissive cloud, the height of the transmissive cloud is estimated to be too low by as much as 100 hPa (Menzel et al. 1992). The largest error occurs when the underlying opaque layer is in the middle troposphere (400–700 hPa) and the upper-cirrus layer is very thin. The error is small when the opaque cloud is near the surface or close to the upper-transmissive layer. The error in effective emissivity of the transmissive cloud increases as the opaque layer approaches the transmissive layer; when they are coincident, the effective emissivity is set to 1.

The processing procedure is outlined briefly here. More details are given in appendix A. Carbon dioxide slicing cloud-top pressures are calculated when the cloud forcing (clear minus cloudy radiance is greater than five times the instrument noise level); otherwise, the infrared window temperature is used to determine an opaque cloud-top pressure. Fields of view are determined to be clear if the moisture corrected 11.1- μ m brightness temperature is within 2.5°C of the known surface temperature. [Over land this is inferred from the National Meteorological Center (NMC) Medium Range Forecast (MRF) model analysis; over the oceans this is the National Oceanic and Atmospheric Administration (NOAA) National Environmental Satellite Data and Information Service (NESDIS) sea surface temperature analysis.]

In this four-year study, HIRS data from *NOAA-10*, *NOAA-11*, and *NOAA-12* are sampled to include only data from every third FOV on every third line with a zenith angle less than 10°. With two satellites, about one-half of the earth is sampled each day. Morning orbits over land are rejected from the data because a good guess of the morning land surface temperature is unavailable, and therefore, discerning cloudy from clear FOVs is difficult. In the Arctic and Antarctic, the HIRS bands are inspected for the presence of surface temperature inversions, which are assumed to be indicators of clear sky.

3. Global cloud statistics

A statistical summary of over 15 million cloud observations from HIRS between June 1989 through May 1993 is shown in Table 1. High clouds above 400 hPa constitute 24% of the observations. Twenty-seven percent of the observations are of clouds between 400 and 700 hPa. Low clouds below 700 hPa are found 26% of the time. Cloud-free conditions are found 23% of the time. Cirrus and transmissive clouds (with effective

TABLE 1. HIRS four-year global cloud statistics (June 1989–May 1993) of the frequency of cloud observations for different heights and effective emissivities N_e . Here $N_e < 0.25$ corresponds to infrared optical depth $\tau < 0.3$; $N_e < 0.5$, $\tau < 0.7$; $N_e < 0.75$, $\tau < 1.4$; and $N_e < 0.95$, $\tau < 3.0$. Percentages are of the total number of observations, clear and cloudy combined. Clouds were not detected in 23.4% of the observations.

Level	All clouds	Effective emissivity (%)				
		<0.25	<0.50	<0.75	<0.95	>0.95
<200 hPa	3.5%	1.2	0.4	0.3	0.7	0.9
<300 hPa	9.6	2.3	1.9	1.6	2.1	1.7
<400 hPa	10.8	2.5	2.3	2.2	2.4	1.4
<500 hPa	11.0	2.3	2.5	2.6	2.5	1.1
<600 hPa	8.2	1.4	2.2	2.5	0.7	1.4
<700 hPa	7.8	0.6	1.2	1.7	0.7	3.6
<800 hPa	7.6	0.2	0.4	0.4	0	6.6
<900 hPa	11.5	0	0	0	0	11.5
<1000 hPa	6.8	0	0	0	0	6.8
Total	76.8	10.5	10.9	11.3	9.1	35.0

emissivities less than 0.95) are found in 42% of our observations; they range from 100 to 800 hPa. The 12% transmissive observations below 500 hPa are most likely broken clouds. Clouds opaque to infrared radiation (with effective emissivities greater than 0.95) are found 35% of the time. The global average cloud effective emissivity (global average of N_e) is found to be 0.54; Warren et al. (1988) report a global cloud fraction of 0.61 from ground observations.

The frequency of different cloud observations is used to indicate the probability that a given HIRS FOV is found to contain a certain type of cloud. The frequency of all clouds over land is 67% versus 79% over ocean; the frequency of cirrus clouds over land is 39% versus 43% over ocean. High clouds above 500 hPa prefer land over ocean (37% versus 34%). Thin clouds ($N_e < 0.50$ or infrared optical depth $\tau < 0.7$) prefer ocean over land (22% versus 18%).

As the satellite views from above the atmosphere, high clouds are found in preference to low clouds. Broken low cloud fields are reported as opaque low clouds because the CO_2 slicing technique is unable to estimate the cloud fraction below the sensitivity peaks in the CO_2 bands. Transmissive clouds cover the range of effective emissivities from 0.0 to 0.95 fairly uniformly.

The CO_2 slicing technique is subject to some errors that have been discussed in Menzel et al. (1992). The large observation area (20 km \times 20 km) produces results where transmissive cloud observations are overestimated; cloud edges and clear sky within a FOV are incorrectly estimated to be transmissive clouds in roughly 5% of the FOVs. Conversely, the HIRS lack of sensitivity to very thin clouds in roughly 5% of the FOVs causes transmissive clouds to be incorrectly classified as lower opaque clouds (Wylie and Menzel 1989). And finally, the top-down view of the satellite reveals high clouds in preference to lower occluded

clouds. These errors are largely offsetting. Overall, the frequency of clear-sky observations in Table 1 is believed to be valid within 3%.

A similar multispectral analysis of transmissive clouds was previously published for continental United States using Geostationary Operational Environmental Satellite (GOES)/VAS data (Wylie and Menzel 1989; Menzel et al. 1992). A comparison of the CO_2 slicing analysis of coincident data from both the GOES-VAS and NOAA-HIRS is shown in appendix C. The two analyses find similar frequency of clear sky. However, the HIRS data produce more transmissive cloud observations than the VAS. We suspect that these differences appear because the radiance noise of the HIRS is less than that of the VAS, and hence, HIRS cloud parameters for thin clouds will be determined more often from CO_2 slicing and less often from the infrared window. When observed and clear FOV radiance observations differ by less than five times the noise in the radiometric measurements, low opaque clouds are inferred. The smaller radiometric noise of the HIRS allows it to produce CO_2 slicing solutions for thin clouds more consistently. In addition, the larger HIRS FOV reduces the ability of the HIRS to find breaks or holes in the upper-level cloud fields. The VAS with a smaller FOV is able to report more of these holes, whereas the HIRS averages them with the cloud field. These two differences would cause the HIRS to indicate more transmissive clouds than the VAS.

Comparison with the results of the International Satellite Cloud Climatology Project (ISCCP) reveal that this HIRS multispectral analysis is finding roughly twice as many transmissive clouds as the ISCCP visible and infrared window analysis. Jin and Rossow (1994) studied collocated ISCCP and HIRS results for four months (July 1989, October 1989, January 1990, and April 1990); HIRS finds 76% cloud cover (80% over water and 65% over land), while ISCCP finds 63% cloud cover (68% over water and 51% over land). Most of this difference is attributed to HIRS detection of optically thin clouds (infrared optical depth less than 0.7); HIRS finds 17% while ISCCP finds only 7%. However, HIRS finds about 3% less low opaque cloud than ISCCP (22% versus 25%, respectively). Hartmann et al. (1992) present one year (March 1985–February 1986) of ISCCP data and find semitransparent cloud (visible optical depth less than 9.4, which corresponds roughly to infrared optical depth less than 4.7) 21% of the time; HIRS finds 42% in the four years of this study (June 1989–May 1993). HIRS finds twice as much semitransparent cloud as ISCCP high in the atmosphere (21% to 10%, respectively) and at midlevels (21% to 11%, respectively). HIRS finds less opaque cloud at high and middle levels above 700 hPa than ISCCP (10% to 15%, respectively), but the low-cloud detection is comparable (25% to 26%, respectively). HIRS finds less clear sky in the four years than the one year of ISCCP that Hartmann et al. (1992) studied (23% to

TABLE 2a. The HIRS global cloud cover from all four years (June 1989–May 1993). Here N_e refers to effective emissivity, and τ refers to the corresponding infrared optical depth. Numbers are frequency of cloud cover; over 15 000 000 observations are included.

Level	None	Effective emissivity (IR optical depth)		
		Thick		
		Thin	$0.5 < N_e$ < 0.95	Opaque
		$N_e < 0.50$ $\tau < 0.7$	$0.7 < \tau$ < 3.0	$N_e > 0.95$ $\tau > 3.0$
High < 400 hPa		11	9	4
Middle < 700 hPa		10	11	6
Low < 1000 hPa		1	0	25
Total	23 (Clear)	42 (Cirrus)		35 (Opaque)

36%, respectively). Both of these comparisons point to the ISSCP difficulty in detecting thin transmissive clouds; if one were to exclude clouds with infrared optical depths less than 0.7 from the HIRS data (roughly 20% of the observations) and increase the frequency of low opaque clouds in the HIRS data (adding roughly 5%), all adjusted HIRS cloud categories would agree with Jin and Rossow (1994) and Hartmann et al. (1992) to within a few percent.

4. Seasonal and geographical trends

Table 2 presents the seasonal variation of clouds by classifications of clear sky, thin clouds ($N_e < 0.5$), thick clouds ($0.5 < N_e < 0.95$), and opaque clouds ($N_e > 0.95$) and by height categories of high (cloud pressure less than 400 hPa), middle (cloud pressure between 400 and 700 hPa), and low (cloud pressure greater than 700 hPa). The all-season four-year summary is also included for comparison. Little variation is found in the global boreal summer versus winter cloud statistics. A few percent more cirrus and less clear sky are found in the boreal winter. Hartmann et al. (1992) report similar seasonal statistical differences.

Figure 1 shows the geographical distribution of cirrus clouds in the summer and winter seasons (darker regions indicate more frequent cloud occurrence). The months of December, January, and February were summarized for the boreal winter (austral summer) and the months of June, July, and August were used for the boreal summer (austral winter). The seasonal summaries were compiled using a uniformly spaced grid of 2° latitude by 3° longitude. Each grid box for each season has at least 500 observations.

The major features of the four-year summary have not changed appreciably from those reported in the two-year summary (Wylie and Menzel 1991). The intertropical convergence zone (ITCZ) is readily discernible as the region of more frequent cirrus (darker

TABLE 2b. The HIRS global cloud cover in the boreal summer from all four years (June 1989–May 1993). Here N_e refers to effective emissivity, and τ refers to the corresponding infrared optical depth. Numbers are frequency of cloud cover; over 3 300 000 observations are included.

Level	No	Effective emissivity (IR optical depth)		
		Thick		
		Thin	$0.5 < N_e$ < 0.95	Opaque
		$N_e < 0.50$ $\tau < 0.7$	$0.7 < \tau$ < 3.0	$N_e > 0.95$ $\tau > 3.0$
High < 400 hPa		11	9	4
Middle < 700 hPa		10	10	5
Low < 1000 hPa		0	0	26
Total	25 (Clear)	40 (Cirrus)		35 (Opaque)

band in the Tropics); the midlatitude storm belts are also evident. The ITCZ is seen to move north with the sun. This seasonal migration is also apparent in the latitudinal summaries shown in Fig. 2. The subtropical high pressure systems are seen in the region of less frequent cirrus cover (white band in the subtropics). Over the Indonesian region, the ITCZ expands in latitudinal coverage from boreal winter to summer. In the central Pacific Ocean, the ITCZ shows both a southern and northern extension during the boreal winter months.

In the Southern Hemisphere, the eastern Pacific Ocean off South America and the eastern Atlantic Ocean off Africa remain relatively free of cirrus clouds throughout the year. The Southern Hemispheric storm belt is evident throughout the year. In the Northern Hemisphere midlatitude storm belts, the frequency of cirrus clouds increases during the winter with the

TABLE 2c. The HIRS global cloud cover in the boreal winter from all four years (June 1989–May 1993). Here N_e refers to effective emissivity, and τ refers to the corresponding infrared optical depth. Numbers are frequency of cloud cover; over 3 600 000 observations are included.

Level	No	Effective emissivity (IR optical depth)		
		Thick		
		Thin	$0.5 < N_e$ < 0.95	Opaque
		$N_e < 0.50$ $\tau < 0.7$	$0.7 < \tau$ < 3.0	$N_e > 0.95$ $\tau > 3.0$
High < 400 hPa		11	10	4
Middle < 700 hPa		10	11	7
Low < 1000 hPa		0	0	24
Total	23 (Clear)	42 (Cirrus)		35 (Opaque)

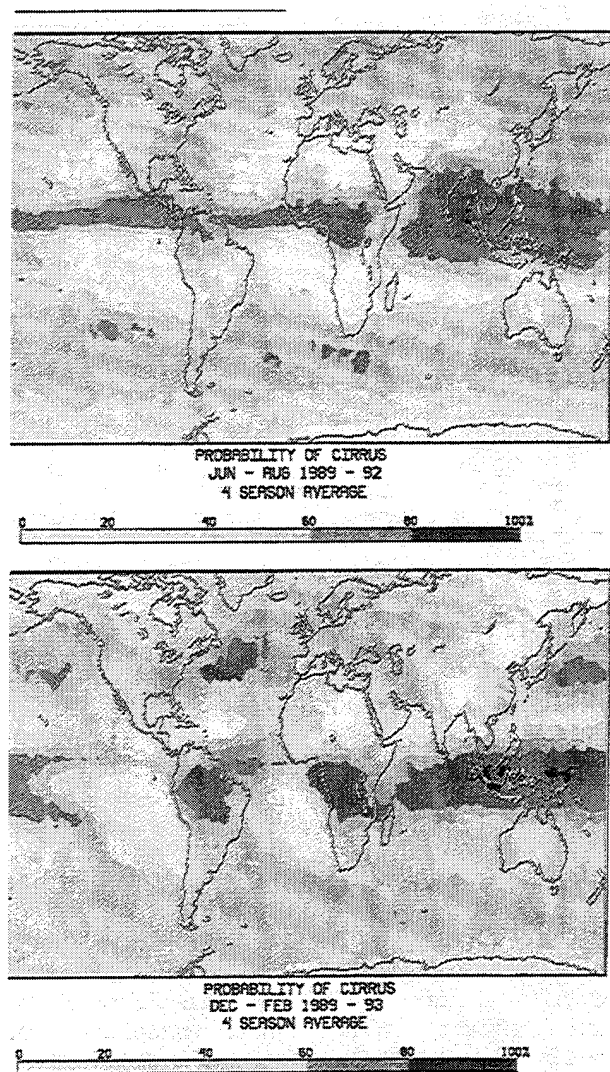


FIG. 1. (a) The geographic frequency of transmissive clouds for the boreal summers (June, July, August) during the observation period June 1989 through May 1993. The left margin of the figure coincides with the international date line. (b) The geographic frequency of transmissive clouds for the boreal winters (December, January, and February) during the observation period June 1989 through May 1993.

strengthening of the Aleutian low in the North Pacific Ocean and the Icelandic low in the North Atlantic Ocean. The North American cirrus cloud cover shows little seasonal change, agreeing with a previous GOES/VAS analysis (Menzel et al. 1992). Large convective development occurs during the austral summer (boreal winter) in South America and Africa, which is readily apparent in the increased occurrence of high-cirrus clouds.

A large seasonal change is found over Antarctica, where few clouds of any altitude are reported in the austral winter. The HIRS data do not show polar stratospheric clouds that occur commonly over Antarctica in the months of June, July, and August. Polar

stratospheric clouds apparently do not attenuate the HIRS bands sufficiently to mask out the strong inversions below them.

These seasonal changes in geographical distribution of global transmissive clouds are largely in agreement with the one-year ISSCP results shown in Hartmann et al. (1992). The ITCZ expands in the Indonesian region in the boreal summer, the Icelandic low creates more cirrus in the boreal winter, convective development in South America and Africa is obvious in the austral summer, and the eastern Atlantic and Pacific Oceans in the Southern Hemisphere stay mostly free of cirrus clouds year-round. As discussed previously, the ISSCP data indicate about half the transmissive clouds that the HIRS data does.

Upper-tropospheric clouds (above 500 hPa) are discussed in the following paragraphs. Figure 2 shows the zonal distribution of high clouds, which includes both the transmissive and opaque clouds (30% and 5% of all observations, respectively). The frequent occurrence of high clouds in the ITCZ is prominent as the central maximum; the midlatitude storm belts are evident in the secondary maxima. Seasonal shifts in the ITCZ are apparent over both land and ocean as the ITCZ moves north and south with the sun. The frequency of high

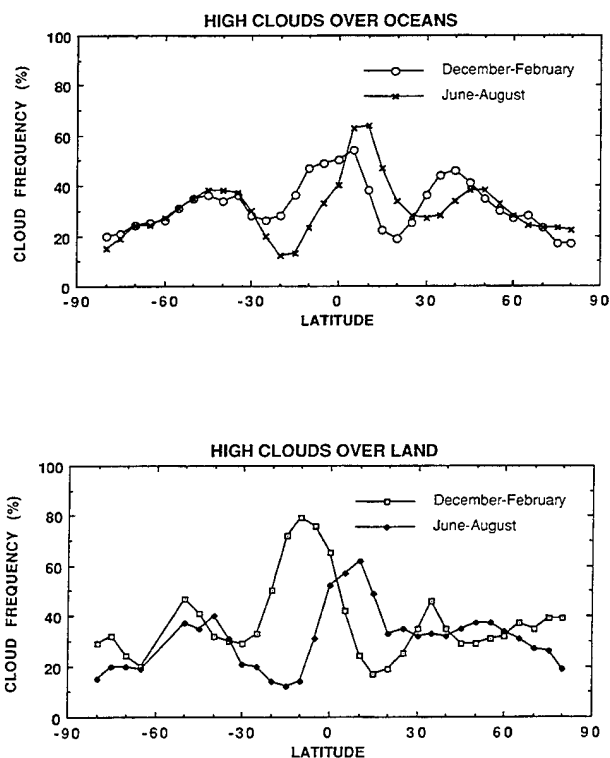


FIG. 2. The frequency of high clouds (cloud pressure < 500 hPa) over ocean is shown in the upper panel as a function of latitude for the boreal summers (June, July, August) of 1989-92 and winters (December, January, February) 1989-93 expressed as a fraction of all satellite observations, clear and cloudy combined. The same over land is shown in the lower panel.

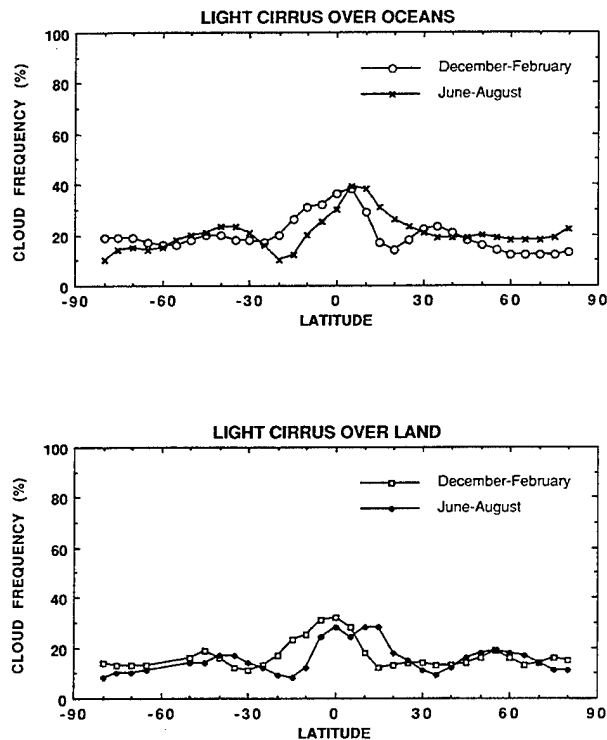


FIG. 3. The frequency of thin transmissive clouds ($N_e < 0.5$, $\tau < 0.7$) over ocean is shown in the upper panel as a function of latitude as a fraction of all satellite observations, clear and cloudy combined. Land is shown in the lower panel.

clouds over land increases strongly from the equator to 30°S during the austral summer. The main contributors are the Amazon Basin of South America and the Congo of Africa. The high clouds over the Southern Hemispheric storm belt, primarily over the oceans from 30° to 70°S, remain constant throughout the year. The Northern Hemispheric landmasses from 45° to 65°N also show little seasonal change in high-cloud cover. Jin and Rossow (1994) indicate that the HIRS zonal

TABLE 3a. The change in HIRS global cloud cover from year 1 (June 1989–May 1990) to year 2 (June 1990–May 1991). Here N_e refers to effective emissivity, and τ refers to the corresponding infrared optical depth. Numbers are frequency of cloud cover in summer and winter of year 2 minus the same in year 1; negative numbers indicate a decrease in cloudiness while positive numbers indicate an increase.

Level	Effective emissivity (IR optical depth)		
	Thin	Thick	Opaque
	$N_e < 0.50$ $\tau < 0.7$	$0.5 < N_e < 0.95$ $0.7 < \tau < 3.0$	$N_e > 0.95$ $\tau > 3.0$
High < 400 hPa	0	1	-1
Middle < 700 hPa	0	-1	0
Low < 1000 hPa	0	0	0
Total	0	0	-1

TABLE 3b. The change in HIRS global cloud cover from year 2 (June 1990–May 1991) to year 3 (June 1991–May 1992). Numbers are frequency of cloud cover in summer and winter of year 3 minus the same in year 2.

Level	Effective emissivity (IR optical depth)		
	Thin	Thick	Opaque
	$N_e < 0.50$ $\tau < 0.7$	$0.5 < N_e < 0.95$ $0.7 < \tau < 3.0$	$N_e > 0.95$ $\tau > 3.0$
High < 400 hPa	4	1	0
Middle < 700 hPa	2	1	-2
Low < 1000 hPa	0	0	-5
Total	6	2	-7

distribution of high cloud is in very good agreement with the ISSCP data, when clouds with infrared optical depth less than 0.7 are omitted from the HIRS data.

Light cirrus show smaller seasonal changes. The latitudinal distribution of thin transmissive ($N_e < 0.5$ or infrared optical depth $\tau < 0.7$) clouds over ocean and over land is shown in Fig. 3. The occurrence is somewhat more likely over the ocean; this disagrees with Warren et al. (1988), who found more cirrus over land than ocean in their ground-based observations. A modest peak from 10°S to 10°N is evident over both land and ocean. Thin transmissive clouds appear globally with a frequency of 5%–40%.

5. Trends in the four years

The progression of cloud cover from year 1 (June 1989–May 1990) to year 2 (June 1990–May 1991), from year 2 to year 3 (June 1991–May 1992), and from year 3 to year 4 (June 1992–May 1993) is shown in Table 3. Thin cloud refers to $N_e < 0.5$ (infrared optical depth $\tau < 0.7$) and thick refers to $0.5 < N_e < 0.95$ ($0.7 < \tau < 3.0$). The change from year 1 to year 2 is imperceptible. The change from year 2 to year 3 is large and very obvious; opaque clouds decrease by 7% and cirrus increases by 8%. Cirrus appears much

TABLE 3c. The change in HIRS global cloud cover from year 3 (June 1991–May 1992) to year 4 (June 1992–May 1993). Numbers are frequency of cloud cover in summer and winter of year 4 minus the same in year 3.

Level	Effective emissivity (IR optical depth)		
	Thin	Thick	Opaque
	$N_e < 0.50$ $\tau < 0.7$	$0.5 < N_e < 0.95$ $0.7 < \tau < 3.0$	$N_e > 0.95$ $\tau > 3.0$
High < 400 hPa	0	0	0
Middle < 700 hPa	2	-1	0
Low < 1000 hPa	0	0	2
Total	2	-1	2

more frequently in the year 3 data than in previous years; conversely opaque cloud appears much less frequently. The probability of clear sky remains stable. The change from year 3 to year 4 is small; cloud cover increases by approximately 3%.

The geographical distribution of the difference in the probability of cirrus occurring in the boreal summer of 1990 minus boreal summer 1989 is shown in Fig. 4a (upper-left panel). Differences greater than 12% are scattered about, with no discernible pattern. Coherent changes are apparent only in the Timor Sea off the northwest coast of Australia (where a decrease of cirrus occurs) and in the Pacific Ocean east of Papua New Guinea (where an increase of cirrus occurs). Figure 4b shows the corresponding difference for the boreal winters of 1990/91 minus 1989/90 (upper-left panel). Again there is not very much difference. The only features are the increase of cirrus in the Coral and Timor Seas and the decrease of cirrus in the Indian Ocean west of Australia (representing a westward shift from Fig. 4a).

A change in cirrus coverage in the summer of 1991 with respect to the summer of 1990 is obvious (Fig. 4a upper-right panel). Coherent increases of cirrus greater than 12% are apparent along the southern edge of the ITCZ, in the southern midlatitudes, the Indian Ocean, and eastern Africa. Decreasing cirrus is indi-

cated in the higher latitudes of the Southern Hemisphere. The boreal winter 1991/92 shows an even stronger increase in cirrus with respect to the winter 1990/1991 (Fig. 4b upper-right panel). The largest increases are in the central Pacific Ocean, the Indian Ocean, and the Northern Hemisphere midlatitudes. The central Pacific Ocean is also the location of an El Niño event where sea surface temperature anomalies greater than 2.0°C were reported in January 1992.

The patterns of increasing cirrus in the boreal summer 1991 are consistent with the decrease in net radiation from the Earth Radiation Budget Experiment (ERBE) for August 1991 observations compared to the August average for the previous five years, especially over the Amazon, the central Atlantic Ocean, the African Congo, off the east African coast, the southern Indian Ocean, and the central Pacific Ocean (Minnis et al. 1993). In this HIRS study, more thin cirrus was found after the eruption of Mt. Pinatubo at the expense of opaque cloud. This is consistent with the hypothesized indirect effect of aerosols, which would cause more high thin cirrus cloud to be produced and to be longer lasting (Sassen 1992).

In the fourth summer of this study, a slight cirrus decrease (Fig. 4a, lower-left panel) is found in the southerly latitudes (50° – 75°S) and in the Atlantic Ocean off the east coast of Africa. Elsewhere there is

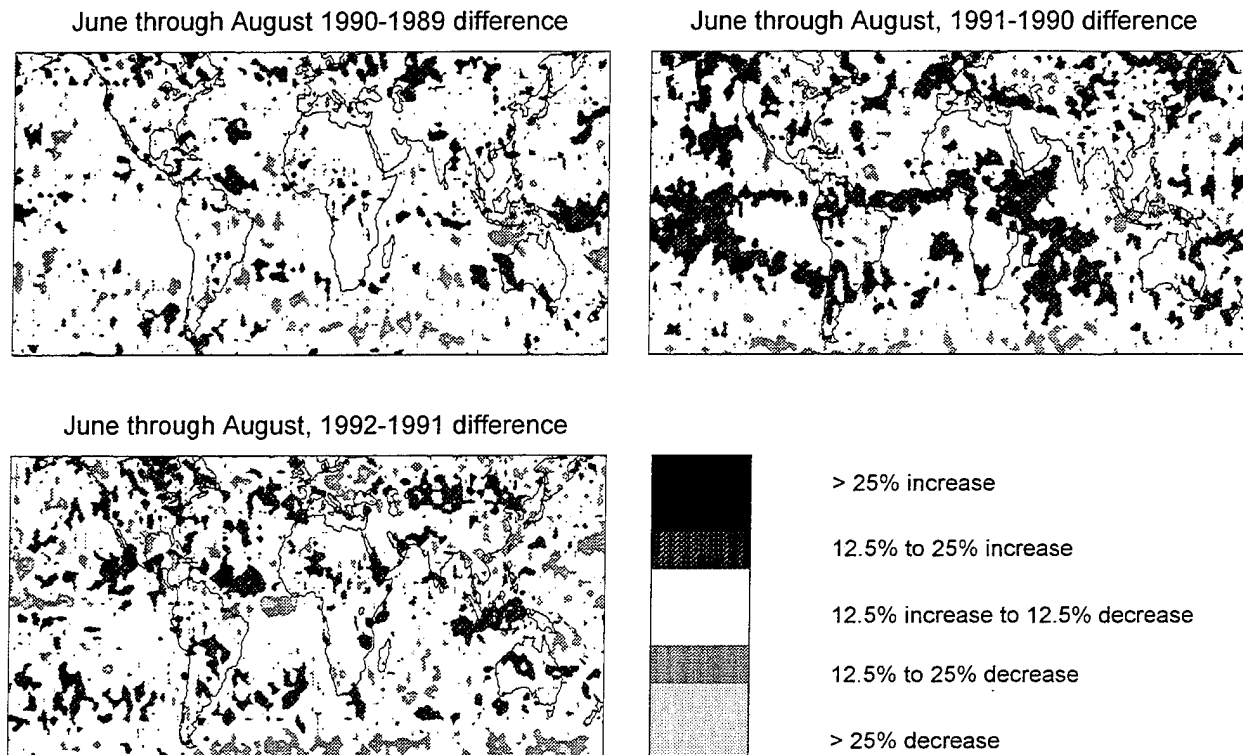


FIG. 4. (a) The geographical distribution of the difference in the probability of cirrus in the four boreal summers, 1990 minus 1989 (upper-left panel), 1991 minus 1990 (upper-right), and 1992 minus 1991 (lower-left). The boreal summer includes the months of June, July, and August.

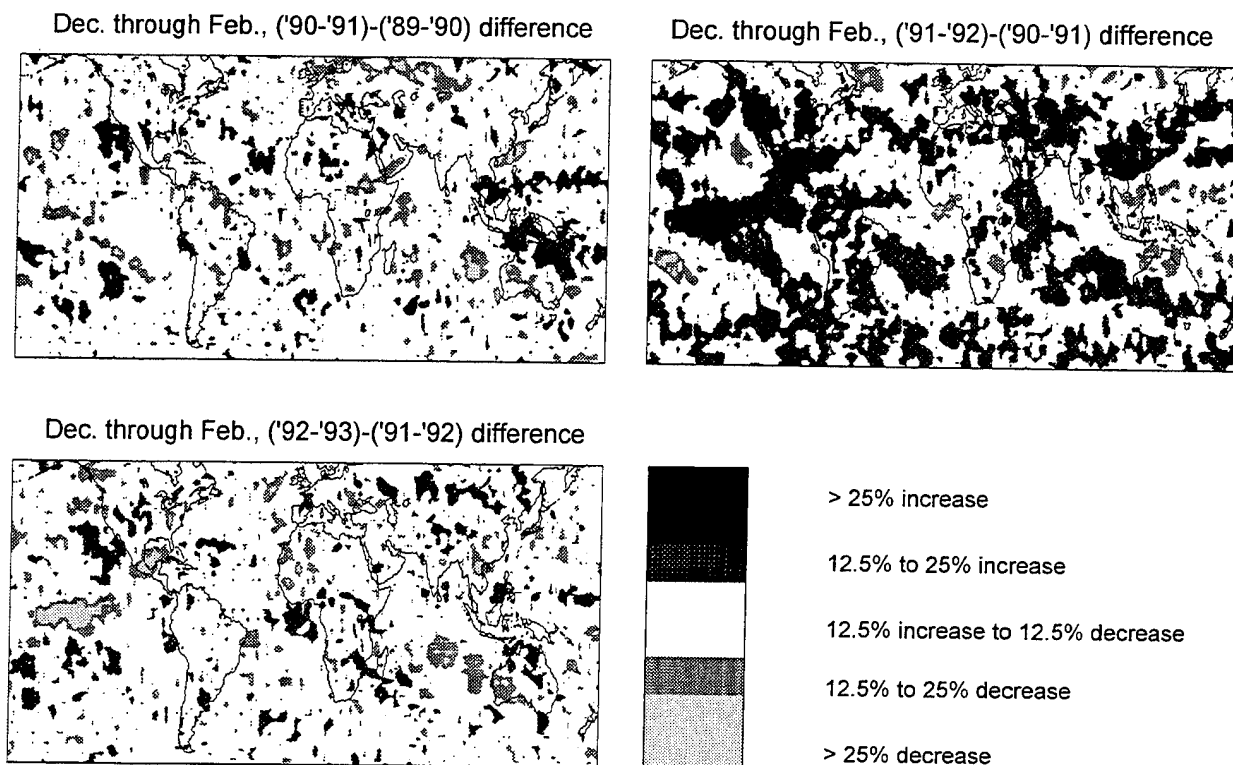


FIG. 4. (b) The geographical distribution of the difference in the probability of cirrus occurring in the four boreal winters. Winter 1990/91 minus winter 1989/90 (upper-left panel), winter 1991/92 minus 1990/91 (upper-right panel), and winter 1992/93 minus 1991/92 (lower-left panel). Boreal winter includes the months of December, January, and February.

no recognizable pattern. Finally, Fig. 4b (lower-left panel) shows the difference for the boreal winters 1992/93 minus 1991/92. Cirrus probability decreases noticeably in the central Pacific Ocean (the location of a dramatic increase in sea surface temperature the previous winter), in the Gulf of Mexico and Central America (in contrast to the increase in the previous year), and off the west coast of Australia in the Indian Ocean (again the location of a noticeable increase the previous year). This last winter appears to be compensating for the local increases in cirrus from the previous winter.

The cirrus increase in 1991 (year 2 to year 3) is in concert with two major global events that affected most climatic data. They are summarized in Halpert and Ropelewski (1993). The first major event started in April 1991, when an increase in eastern Pacific Ocean temperatures signaled the start of an El Niño–Southern Oscillation (ENSO) event. Subsequently, by October 1991, outgoing longwave radiation (OLR) measurements from satellites and 850-hPa wind observations showed large anomalies from climatic means. By January 1992, sea surface temperature anomalies in the eastern equatorial Pacific Ocean were greater than 2.0°C (Kousky 1992). The second major event came in June 1991 with the eruption of Mt. Pinatubo, which set new records for

ash and aerosol in the stratosphere. Aerosol optical-depth measurements by Stowe et al. (1992) showed a dramatic increase in the Tropics in the following months. This aerosol later spread to higher latitudes by the end of the year.

Figure 5 shows the monthly changes in these HIRS high-cloud data for the four years. A major increase in global high clouds (solid line in Fig. 5) begins in April 1991, coincident with the change in eastern Pacific Ocean temperatures. The frequency of high-cloud observations (above 500 hPa) increases from 32% in March 1991 to 37% in June 1991 to 39% in December 1991. The largest high-cloud increases are in the Tropics (20°S to 20°N). Tropical high-cloud frequency increases from 34% in March 1991 to 40% in June 1991 (long dash in Fig. 5), while tropical light cirrus ($N_e < 0.5$ or $\tau < 0.7$) increases even more from 23% in March 1991 to 31% in June 1991 (short dash in Fig. 5). Examination of the local region in the eastern Pacific Ocean (10°S to 10°N , 110°W to 170°W) reveals even more dramatic changes (dot-dash in Fig. 5). Light cirrus observations change from near 25% frequency during the winter to over 40% in the summer. Seasonal and monthly changes are evident. In the boreal winter (December 1991 to February 1992) frequencies of 55%–60% are found, well in excess of the previous years.

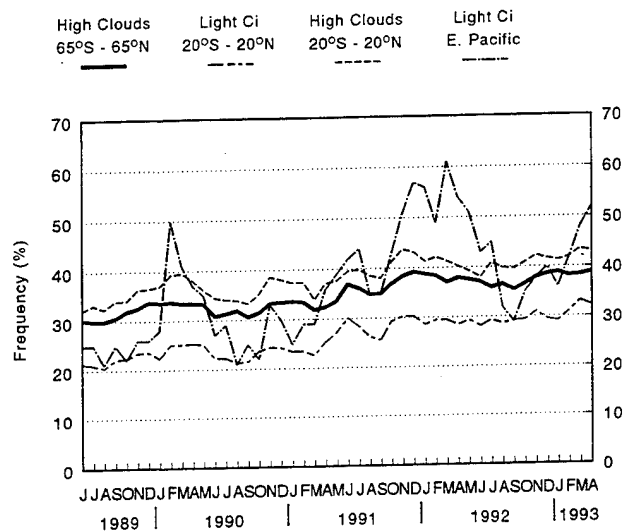


FIG. 5. Monthly time series of high cloud (over 500 hPa) observations from 65°S to 65°N latitude (solid line); light cirrus with $N_e < 0.5$, $\tau < 0.7$ in the Tropics from 20°S to 20°N (triple dash); all high clouds (over 500 hPa) in the Tropics, 20°S to 20°N (dash); and light cirrus ($N_e < 0.5$, $\tau < 0.7$) in the eastern Pacific Ocean from 10°S to 10°N, 110° to 170°W (dash dot).

Changes in the satellite system are not the cause of the increased detection of cirrus and high cloud. In June 1991, *NOAA-12* replaced *NOAA-10* as the sunrise and sunset satellite. *NOAA-11*, the midday and midnight satellite, maintained continuous operation through this entire four-year period. Examination of *NOAA-11* data reveals only the same changes. Thus, we conclude that the change in satellites had no effect on the trends evident in this data. The increase in stratospheric aerosol also should not have affected the cloud observations. The CO₂ sounding bands are in the 13–15 μm region of the infrared spectrum, which is beyond the portion of the spectrum affected by these very small stratospheric particles (Ackerman and Strabala 1994).

It is also significant that the increase in cirrus and high-cloud observations continue into 1993 with reduction only in small areas. The other climatic indicators, such as the eastern Pacific Ocean temperatures, OLR, and 850-hPa wind anomalies, revert back to near-normal (average) levels by July 1992. The increased detection of cirrus in the HIRS data persists beyond 1992 into 1993. We do not have an explanation for this persistence but suggest that forces that cause and maintain cirrus [as described in Menzel et al. (1992)] are subtle and could be present even after other climatic anomalies have subsided.

6. Diurnal trends

Diurnal variations in cloud cover are examined using the four observations from the two NOAA satellites each day. *NOAA-11* passes over a given location at

approximately 0200 to 0300 LT and 1400 to 1500 LT (midnight and midday) every day while *NOAA-10* and *NOAA-12* have an overpass from 0700 to 0800 LT and 1900 to 2000 LT (sunrise and sunset). These observations are analyzed in four time blocks of six hours each. Differences in the frequency of cloud observations from the daily mean are presented in Fig. 6. The diurnal anomalies are expressed as the difference of the frequency of observation of cloud from the mean frequency using all observations at all times. Diurnal variations in cloud cover are discussed only over water. Over land, two of the four satellite passes are not analyzed each day because the NMC model analysis does not track the strong diurnal variations in surface temperatures, especially in many desert areas. Over the ocean, the diurnal surface temperature change is presumed to be insignificant and the same NOAA/NESDIS sea surface temperature analysis is used for each satellite pass in this cloud analysis.

A diurnal cycle in all cloud observations (Fig. 6), both cirrus and lower-altitude cloud forms, is found mainly outside of the ITCZ. Maxima occur in the midnight overpass. Geographical diurnal variations (not shown) are strongest in the southeastern Atlantic and Pacific Oceans. Some variations are present in the

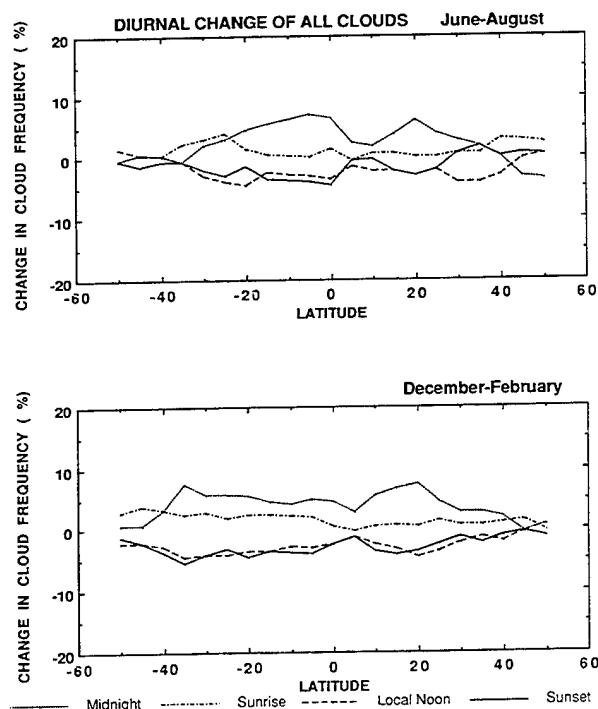


FIG. 6. The diurnal change from the seasonal mean of all cloud observations expressed as a change in percentage points of the total clear and cloudy observations. Midnight represents the *NOAA-11* evening pass that actually occurred between 0100 and 0300 LT. Sunrise is the morning *NOAA-10* or *NOAA-12* pass nominally from 0700 to 0800 LT. Local noon is the afternoon *NOAA-11* pass from 1300 to 1500 LT. Sunset is the evening *NOAA-10* or *NOAA-12* pass from 1900 to 2000 LT.

northeastern Pacific Ocean, near the coasts of California and Baja, and in the central Atlantic Ocean to the African coast. The cycle appears to be stronger during the summer and is dominated by lower-cloud forms, mostly marine stratus.

High clouds (above 500 hPa) show little diurnal pattern (see Fig. 7). The frequency of these clouds changes by ± 3 percentage points during the day at all latitudes. The largest diurnal variation is found near the ITCZ from the equator to 15°N in the boreal summer. Thin cirrus ($N_e < 0.5$ or $\tau < 0.7$) exhibit even smaller diurnal variations with no obvious pattern.

7. Summary and conclusions

There continues to be a global preponderance of transmissive clouds 42% on the average for the four years covered by June 1989 to May 1993. About three-fourths of these are above 500 hPa and presumed to be cirrus. In the ITCZ, a high frequency of cirrus (greater than 50%) is found at all times; a modest seasonal movement tracks the sun. Large seasonal changes in cloud cover occur over the oceans in the storm belts at midlatitudes; the concentrations of these clouds migrate north and south with the seasons following the progressions of the subtropical highs (anticyclones). More cirrus is found in the summer than in the winter in each hemisphere (largely due to the ITCZ).

Large changes in cirrus and high cloud cover are found beginning in the spring-summer 1991. These cloud frequency increases occur in concert with the 1991/92 ENSO and the Mt. Pinatubo volcanic eruption. Associated changes include an increase in sea surface temperature starting April 1991, anomalies in outgoing longwave radiation and 850-hPa winds around October 1991, and a dramatic increase in stratospheric aerosol after June 1991. The cirrus and high-cloud increase starts before Mt. Pinatubo's eruption and persists beyond the summer of 1992, at which time the ENSO anomalies are mostly gone and stratospheric aerosol measurements are near their preeruption levels. Decreases in cirrus are seen in local regions, but higher occurrence of cirrus in the global average remains. There is no obvious explanation other than thin cirrus are statistically persistent and do not exhibit large seasonal changes outside of the Tropics, whereas other cloud forms do show large seasonal variations.

The increase in cirrus and high cloud is accompanied by a corresponding decrease in satellite observations of lower-altitude opaque clouds; overall cloudiness changed very little during this period. Obviously, a satellite detects lower cloud forms less when higher clouds become more prevalent. However, the trend reported in this paper of more transmissive high cloud and less low opaque cloud is loosely supported by appreciable decreases in precipitation in many regions of the world (Halpert and Ropelewski 1993) during the 1991/92 ENSO and volcanic period.

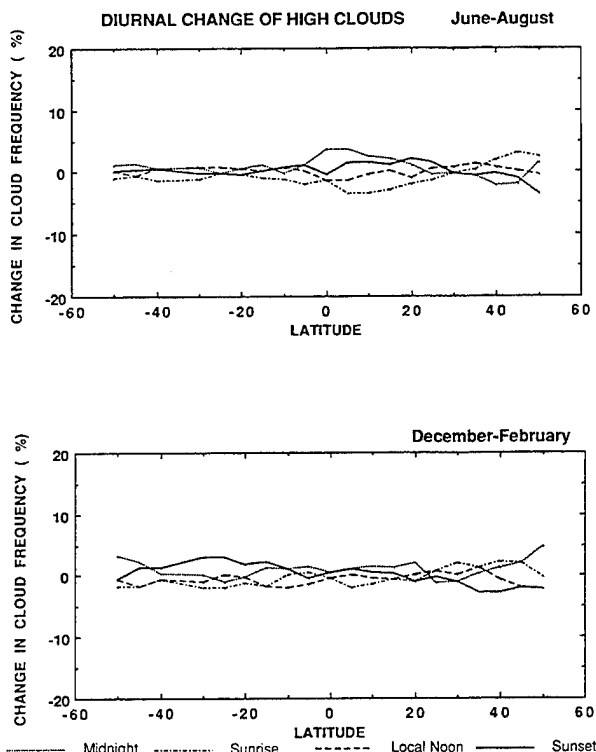


FIG. 7. Same as Fig. 6 for the change in the frequency of high cloud observations (pressure < 500 hPa).

A similar increase in cloud cover also was reported in the 1982/83 ENSO by Weare (1992) using the *Nimbus-7* infrared analysis of Stowe et al. (1988). An increase in both the amount of cloud (all altitudes) and the average cloud height was found. The height increase indicated more high cloud in late 1982 and most of 1983 during the height of the ENSO. This is a similar trend that this HIRS analysis finds for the 1991/92 ENSO. We have no explanation for these changes in global cloud cover. This is the topic of future studies.

Acknowledgments. This work was supported by Grants N00014-85-K-0581 and N00014-87-K-0436 of the Office of Naval Research; Grant NAG1-553 and Contract NAS5-31367 from the National Aeronautics and Space Administration; Grant ATM-8703966 from the National Science Foundation; Contract 50-WCNE-8-06058 from the National Oceanic and Atmospheric Administration; and Grant F19628-91-K-0007 from the United States Air Force Geophysics Laboratory.

APPENDIX A

Technique Description

The HIRS radiometer senses infrared radiation in 18 spectral bands that lie between 3.9 and $15\ \mu\text{m}$ at 20 – 35 km resolution (depending upon viewing angle)

in addition to visible reflections at the same resolution. The four bands in the CO₂ absorption band at 15 μm are used to differentiate cloud altitudes, and the long-wave infrared window band identifies the effective emissivity of the cloud in the HIRS FOV.

The CO₂ slicing technique is derived from the calculation of radiative transfer in an atmosphere with a single cloud layer. For a single-level cloud element in an FOV, the radiance observed at the satellite $R(\eta)$ in spectral band η can be written

$$R(\eta) = (1 - N\epsilon) \left\{ B[\eta, T(P_s)]\tau(\eta, P_s) + \int_{P_s}^{P_c} \{B[\eta, T(p)]d\tau/dp\} dp \right\} + N\epsilon B[\eta, T(P_c)]\tau(\eta, P_c) + \int_{P_c}^0 \{B[\eta, T(p)]d\tau/dp\} dp, \quad (\text{A1})$$

where $\tau(\eta, P)$ is the transmittance through the atmosphere for band η , $N\epsilon$ is the effective emissivity of the cloud in the FOV, and $B[\eta, T(P)]$ is the Planck function for band η and temperature T at pressure level P ; P_s is the surface pressure, while P_c is the cloud-top pressure. The four terms in Eq. (A1) are the radiation emitted from the surface, the contribution from the atmosphere below the cloud, the cloud contribution, and the contribution from the atmosphere above the cloud. For a clear FOV ($N\epsilon = 0$), the satellite measured radiance R_{clr} is

$$R_{\text{clr}}(\eta) = B[\eta, T(P_s)]\tau(\eta, P_s) + \int_{P_s}^0 \{B[\eta, T(p)]d\tau/dp\} dp. \quad (\text{A2})$$

Subtracting the clear FOV radiance $R_{\text{clr}}(\eta)$ from the cloudy FOV radiance $R(\eta)$ yields the following result:

$$R(\eta) - R_{\text{clr}}(\eta) = -N\epsilon B[\eta, T(P_s)]\tau(\eta, P_s) - N\epsilon \int_{P_s}^{P_c} \{B[\eta, T(p)]d\tau/dp\} dp + N\epsilon B[\eta, T(P_c)]\tau(\eta, P_c). \quad (\text{A3})$$

This is the cloud signal in the satellite measured radiances for spectral band η ; it is the radiance difference of the cloudy FOV from neighboring clear FOVs. A simplified equation, after integration by parts, is

$$R(\eta) - R_{\text{clr}}(\eta) = N\epsilon \int_{P_s}^{P_c} \{\tau(\eta, p)dB[\eta, T(p)]/dp\} dp. \quad (\text{A4})$$

Following the work of Smith and Platt (1978), the ratio of the cloud signal for two spectral bands of frequency η_1 and η_2 viewing the same FOV can be written as

$$\frac{R(\eta_1) - R_{\text{clr}}(\eta_1)}{R(\eta_2) - R_{\text{clr}}(\eta_2)} = \frac{N\epsilon_1 \int_{P_s}^{P_c} \{\tau(\eta_1, p)dB[\eta_1, T(p)]/dp\} dp}{N\epsilon_2 \int_{P_s}^{P_c} \{\tau(\eta_2, p)dB[\eta_2, T(p)]/dp\} dp}. \quad (\text{A5})$$

If the frequencies are close enough together, then $N\epsilon_1$ approximates $N\epsilon_2$, and one has an expression by which the pressure of the cloud (P_c) within the FOV can be calculated without a priori knowledge of the emissivity.

The left side of Eq. (A5) is determined from the satellite-observed radiances in a given FOV and the clear-air radiances inferred from spatial analyses of satellite clear radiance observations. The right side of Eq. (A5) is calculated from a temperature profile $T(p)$ and the profiles of atmospheric transmittance for the spectral bands $\tau(\eta, P)$ as a function of P_c , the cloud-top pressure. The calculation uses global analyses of temperature and moisture fields from the NMC and is performed at 50-hPa intervals from 1000 to 100 hPa. For a given spectral-band pair, the solution for P_c is the best match of observed and calculated ratios.

Once a cloud height has been determined, an effective emissivity (also referred to as effective cloud amount in this paper) is evaluated from the infrared window-band data using the relation

$$N\epsilon = \frac{R(w) - R_{\text{clr}}(w)}{B[w, T(P_c)] - R_{\text{clr}}(w)}. \quad (\text{A6})$$

Here, $N\epsilon$ is the effective cloud amount observed in the window band, w represents the window-band frequency, and $B[w, T(P_c)]$ is the opaque cloud radiance in the window band.

Using the ratios of radiances of the four CO₂ spectral bands, four separate cloud-top pressures can be determined (14.2/14.0, 14.0/13.7, 14.0/13.3, and 13.7/13.3). Whenever $(R - R_{\text{clr}})$ is within five times the noise response of the instrument (conservatively estimated at roughly 1 mW m⁻² ster⁻¹ cm), the resulting P_c is rejected. Using the measured infrared window radiance and the four cloud-top pressures, four calculations of effective emissivity are also made. As described by Menzel et al. (1983), the most representative cloud height and effective emissivity are those that best satisfy the radiative transfer equation for the four CO₂ spectral bands.

If no ratio of radiances can be reliably calculated because $(R - R_{\text{clr}})$ is within five times the instrument noise level, then a cloud-top pressure is calculated directly from the comparison of the HIRS observed 11.1- μm infrared window-band brightness temperature with an in situ temperature profile, and the effective emissivity is assumed to be unity. In this way, all clouds are assigned a cloud-top pressure either by CO₂ or infrared window calculations.

Fields of view are determined to be clear or cloudy through inspection of the 11.1- μm brightness temperature with an 8.3- or 12.0- μm band correction for moisture absorption. The band differences (11.1–8.3 μm for *NOAA-10* and *NOAA-12*, or 11.1–12.0 μm for *NOAA-11*) were used to lower the threshold for clear–cloudy decisions in areas where water vapor affected the window band. This threshold change varied from 0°C near the poles in dry air masses to as high as 7°C in the moist tropical atmospheres. If the moisture-corrected 11.1- μm brightness temperature is within 2.5°C of the known surface temperature (over land this is inferred from the NMC MRF model analysis; over the oceans this is the NOAA/NESDIS sea surface temperature analysis), then the FOV is assumed to be clear ($P_c = 1000$ hPa) and no cloud parameters are calculated.

The HIRS data are calibrated and navigated by NOAA/NESDIS. These data are transmitted daily to the Man computer Interactive Data Access System at the University of Wisconsin–Madison. The HIRS data from *NOAA-10*, *NOAA-11*, and *NOAA-12* are sampled to make the processing more manageable. Every third pixel on every third line is used. The data are also edited for zenith angle, eliminating data over 10° to assure top-down viewing of the clouds and to minimize any problems caused by the increased pathlength through the atmosphere of radiation upwelling to the satellite. The resulting coverage is restricted to approximately the center one-third of the orbit swath. With two satellites, about one-half of the earth is sampled each day.

Morning orbits over land are not used because the surface temperature analysis over subtropical deserts is often warmer than the HIRS data; this causes cloud-free areas to be mistaken as clouds. However, morning orbits over the oceans are used because no diurnal temperature change of the surface is assumed.

In the Arctic and Antarctic, the HIRS bands are inspected for the presence of surface temperature inversions. Over high-altitude areas of Antarctica and Greenland, the HIRS 700-hPa band is often warmer than the window band. We assume that this indicates the presence of surface inversions from radiative cooling under clear skies. Surface inversions normally cannot be seen by the HIRS, but over polar high-altitude continents, the thermal contrast between 700-hPa and the elevated surface is often large enough to be detected. When the 700-hPa band is warmer than the window band, the observation is classified as cloud free. When the 700-hPa band is within 2.0°C of the window band, we assume that both bands saw the top of a cloud and the observation is classified as cloudy.

APPENDIX B

Comparison of AVHRR and HIRS Cloud Fractions

In classifying transmissive cloud observations where the HIRS radiometer detects radiation from below a

cloud layer as well as radiation from the cloud layer itself, we assume that more of the semitransparency for a given field of view is due to cloud emissivity being less than 1 than due to the cloud not completely covering the HIRS 20-km field of view. In order to investigate this assumption more thoroughly, the effective emissivities N_{ϵ_H} from the HIRS CO₂ slicing are compared to cloud fractions N_A inferred from 1-km AVHRR data.

Figure B1 shows the plot of AVHRR cloud fraction N_A (determined from the number of AVHRR FOVs where the moisture-corrected infrared window brightness temperatures is 2°C colder than NOAA/NESDIS sea surface temperature analysis within a collocated HIRS FOV) versus the HIRS CO₂ slicing effective emissivity N_{ϵ_H} . Roughly 100 comparisons are made for data from 6 and 12 January 1994 covering 20°–40°N in the western Atlantic Ocean. (Figure B2 shows the AVHRR infrared window image for 6 January 1994.) FOVs with clouds tops below 700 hPa are not included in the comparison because the CO₂ slicing algorithm is not used below that altitude. These data include subtropical clouds, high clouds from a cold front, and post-cold-frontal clouds.

Three-fourths of the HIRS CO₂ cloud observations are found to be completely cloud covered in the AVHRR data (N_A between 0.90 and 1.00). This is in good agreement with the work of Baum et al. (1992), where 60% of the HIRS FOVs were found to be completely cloud covered in the AVHRR data. The remaining one-fourth of the HIRS cloudy FOVs, where N_A is less than 0.90, have N_{ϵ_H} less than 0.45. It appears that for thick cloud ($N_{\epsilon_H} > 0.50$), the FOV is always completely cloud covered ($N_A = 1.0$); for thin cloud ($N_{\epsilon_H} < 0.50$), the FOV is almost always more than half covered with cloud ($0.50 < N_A < 1.0$). Wielicki

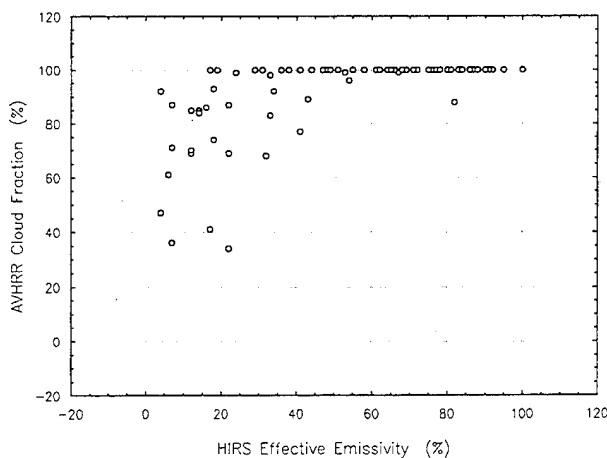


FIG. B1. Plot of AVHRR cloud fraction N_A (determined from infrared brightness temperature comparison to surface temperature within a collocated HIRS FOV) versus the HIRS CO₂ slicing effective emissivity N_{ϵ_H} for 6 and 12 January 1994 over the Atlantic Ocean.

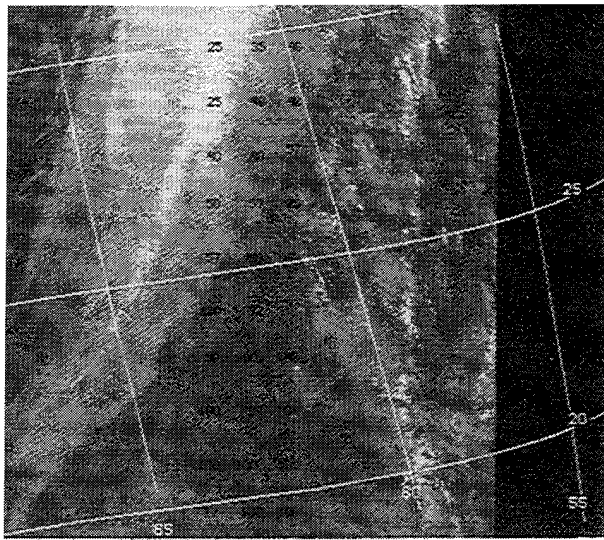


FIG. B2. AVHRR infrared window image from 6 January 1994 over the Atlantic Ocean from which the cloud fraction versus effective emissivity study was made. HIRS CO₂ cloud pressures are indicated in hPa divided by 10.

and Parker (1992) also found that cirrus clouds have considerable spatial coherence and that most of the effect of sensor resolution is very weak on cirrus cloud-cover estimates.

Figure B1 confirms the assertion that cloud emissivity and not cloud fraction is the dominant parameter in FOVs observed to have transmissive clouds. If cloud fraction N dominates and emissivity ϵ of the cloud is not significant in the CO₂ slicing determination, then all points would lie on the $N_A = N\epsilon_H$ line. If ϵ variation from FOV to FOV dominates N variation, then the points would lie on or close to the $N_A = 1.0$ ordinate line. Clearly, for $0.5 < N\epsilon_H < 1.0$, the cloud emissivity is the dominate cause of semitransparency. Cloud fraction causes little change in observed radiance from one FOV to another. For $0.0 < N\epsilon_H < 0.5$, the cloud emissivity is the major cause, but cloud fraction is responsible for some of the variation.

APPENDIX C

Comparison of the NOAA/HIRS and the GOES/VAS Cloud Analyses

The CO₂ slicing technique has been used to process cloud parameters with GOES-VAS data for four years prior to the start of the NOAA/HIRS analysis reported here [see Wylie and Menzel (1989) and Menzel et al. (1992)]. The GOES-VAS algorithm uses the same equations as shown in appendix A. However, there are differences in the data and methods used in handling of the data. 1) The GOES-VAS has three bands in the CO₂ absorption region of the spectrum, whereas the HIRS has four bands; the VAS does not have the 13.7-

μm band that has additional midlevel sensitivity. 2) The GOES-VAS FOV (10×10 km) is smaller than the HIRS FOV (20×20 km); the VAS algorithm averages three FOVs for each cloud determination representing a 300-km^2 observation area and a sample noise of roughly $0.8 \text{ mW m}^{-2} \text{ ster}^{-1} \text{ cm}$, while the HIRS algorithm uses a single FOV representing a 400-km^2 observation area with sample noise roughly $0.2 \text{ mW m}^{-2} \text{ ster}^{-1} \text{ cm}$. 3) Surface topographic heights are used in the HIRS algorithm, while they are not in the VAS algorithm; the surface pressure in Eq. (5) of appendix A is determined from topography for the HIRS solutions, while all VAS solutions assume a surface of 1000 hPa. This affects the VAS results over the Rocky Mountains by 50 hPa or less. 4) A separate sea surface temperature analysis is used in the HIRS processing, while the VAS processing uses the same MRF model surface temperature analysis both over land and water. The VAS land surface temperatures are corrected using the Service A hourly reports, whereas the HIRS are not. This will affect the determination of low cloud with the window band, but it will have almost no effect on CO₂ algorithm solutions since only one of the bands sees the ground.

Single FOV comparisons of HIRS and VAS cloud parameter determinations are attempted. For several days during the 1986 FIRE (First International Satellite Cloud Climatology Project Experiment) in transmissive cloud conditions, over 100 collocated single FOV observations within 15 min were accomplished. Carbon dioxide slicing cloud heights determined by the HIRS are 20 hPa larger (lower altitude) on average than those from the VAS in the single FOV comparison; effective emissivities average 0.05 higher on the VAS than the HIRS. Fluctuations are on the order of 100 hPa for cloud-top pressure and 0.30 for effective emissivity. In this single FOV study, the VAS and HIRS cloud parameters compare within the estimated errors (Menzel et al. 1992). However, these results, while reassuring, must be viewed with some caution. Collocation over the same cloud element is very difficult as the satellite sensors have different FOVs, viewing times, and viewing angles.

A more meaningful comparison of HIRS and VAS cloud analyses is the seasonal average of the frequencies of cloud observations over North America for the four years of the HIRS study (June 1989 to May 1993). Table C1 shows the summary of the four winter seasons (December, January, February) and four summer seasons (June, July, August) of the HIRS cloud observations covering the North American region (29°N to 49°N and 70°W to 130°W) as well as the corresponding seasonal summary of the VAS over the same area and time period. Both HIRS and VAS find roughly the same amount of seasonal cloud cover (70% HIRS and 73% VAS in the summer and 76% HIRS and 78% VAS in the winter). However, HIRS reports more transmissive cirrus in both winter and summer, 45%

TABLE C1a. The HIRS cloud cover in the boreal summer from all four years (June 1989–May 1993) over North America (29° to 49°N, 70° to 130° W). Here N_e refers to effective emissivity, and τ refers to the corresponding infrared optical depth. Numbers are frequency of cloud cover; over 600 000 observations are included.

Level	None	Effective emissivity (IR optical depth)		
		Thick		
		Thin	$0.5 < N_e$ < 0.95	Opaque
		$N_e < 0.50$ $\tau < 0.7$	$0.7 < \tau$ < 3.0	$N_e > 0.95$ $\tau > 3.0$
High < 400 hPa		9	9	6
Middle < 700 hPa		9	8	8
Low < 1000 hPa	30	0	0	21
Total	30	35		35
	(Clear)	(Cirrus)		(Opaque)

HIRS to 33% VAS in winter and 35% HIRS to 27% VAS in summer. In particular, HIRS has 10%–15% more midlevel (400–700 hPa) transmissive observations than the VAS. On the other hand, VAS has 10% more low-level opaque cloud observations. This is caused primarily by the larger noise in the VAS sensor that inhibits CO₂ slicing solutions for smaller cloudy versus clear radiance contrasts and identifies the cloud as low opaque in the infrared window solution.

The geographical distribution of the probabilities of high clouds above 500 hPa in each season computed from VAS and HIRS are presented in Fig. C1. The cloud cover patterns are similar. In the winter, both the HIRS and VAS show higher probability of cloud cover over the Pacific Northwest, the Rocky Mountains, and along the Gulf of Mexico and the eastern shore (40%–60%), while they indicate a lower probability (20%–40%) in the southwest over Baja Mexico.

TABLE C1b. The VAS cloud cover in the boreal summer from all four years (June 1989–May 1993) over North America (29° to 49°N, 70° to 130°W). Here N_e refers to effective emissivity, and τ refers to the corresponding infrared optical depth. Numbers are frequency of cloud cover; over 2 200 000 observations are included.

Level	None	Effective emissivity (IR optical depth)		
		Thick		
		Thin	$0.5 < N_e$ < 0.95	Opaque
		$N_e < 0.50$ $\tau < 0.7$	$0.7 < \tau$ < 3.0	$N_e > 0.95$ $\tau > 3.0$
High < 400 hPa		10	12	3
Middle < 700 hPa		2	3	10
Low < 1000 hPa	27	0	0	33
Total	27	27		46
	(Clear)	(Cirrus)		(Opaque)

TABLE C1c. The HIRS cloud cover in the boreal winter from all four years (June 1989–May 1993) over North America (29° to 49°N, 70° to 130°W). Here N_e refers to effective emissivity, and τ refers to the corresponding infrared optical depth. Numbers are frequency of cloud cover; over 600 000 observations are included.

Level	None	Effective emissivity (IR optical depth)		
		Thick		
		Thin	$0.5 < N_e$ < 0.95	Opaque
		$N_e < 0.50$ $\tau < 0.7$	$0.7 < \tau$ < 3.0	$N_e > 0.95$ $\tau > 3.0$
High < 400 hPa		9	12	5
Middle < 700 hPa		9	15	12
Low < 1000 hPa	24	0	0	14
Total	24	45		31
	(Clear)	(Cirrus)		(Opaque)

There is some disagreement in the northeast where VAS sees 20% more clouds than HIRS; this may be attributed to the large viewing angle of the VAS. In the summer, the cloud cover reduces (down by 20%) along the West Coast and in the southern states, but it persists in the Rocky Mountains and along the eastern shore in both HIRS and VAS. Again there is disagreement in the Northeast, where HIRS now sees 20% more cloud. Some of the moderate disagreement in both seasons over the oceans can be attributed to the difference in the sea surface temperature analysis used for HIRS versus VAS (as mentioned above).

In summary, the HIRS finds more midlevel (400–700 hPa) transmissive clouds and fewer low-level opaque clouds than the VAS but agrees with it in overall cloud reports. The geographical distribution of cloud reports from HIRS is similar to that from VAS, especially when a small VAS view angle is maintained.

TABLE C1d. The VAS cloud cover in the boreal winter from all four years (June 1989–May 1993) over North America (29° to 49°N, 70° to 130°W). Here N_e refers to effective emissivity, and τ refers to the corresponding infrared optical depth. Numbers are frequency of cloud cover; over 2 600 000 observations are included.

Level	None	Effective emissivity (IR optical depth)		
		Thick		
		Thin	$0.5 < N_e$ < 0.95	Opaque
		$N_e < 0.50$ $\tau < 0.7$	$0.7 < \tau$ < 3.0	$N_e > 0.95$ $\tau > 3.0$
High < 400 hPa		10	15	4
Middle < 700 hPa		2	6	20
Low < 1000 hPa	22	0	0	21
Total	22	33		45
	(Clear)	(Cirrus)		(Opaque)

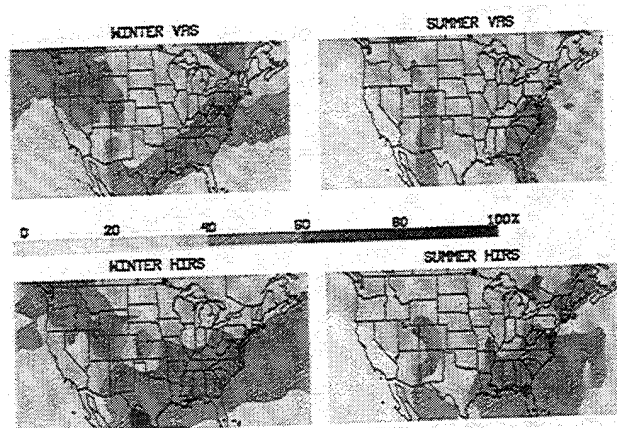


FIG. C1. The frequency of high cloud observations (cirrus and opaque above 500 hPa) reported by VAS and HIRS during four years (June 1989 to May 1993) in the boreal winter months (December, January, and February) and in the boreal summer months (June, July, and August). Gray shades indicate changes of 20%.

REFERENCES

- Ackerman, S. A., and K. I. Strabala, 1994: Satellite remote sensing of H₂SO₄ aerosol using the 8–12 micron window region: Application to Mount Pinatubo. *J. Appl. Meteor.*, submitted.
- Baum, B. A., B. A. Wielicki, and P. Minnis, 1992: Cloud-property retrieval using merged HIRS and AVHRR data. *J. Appl. Meteor.*, **31**, 351–369.
- Chahine, M. T., 1974: Remote sounding of cloudy atmospheres. I: The single cloud layer. *J. Atmos. Sci.*, **31**, 233–243.
- Eyre, J. R., and W. P. Menzel, 1989: Retrieval of cloud parameters from satellite sounder data: A simulation study. *J. Appl. Meteor.*, **28**, 267–275.
- Gruber, A., and T. S. Chen, 1988: Diurnal variation of outgoing longwave radiation. *J. Climate Appl. Meteor.*, **8**, 1–16.
- Halpert, M. S., and C. F. Ropelewski, 1993: *Fourth Annual Climate Assessment, 1992*. U.S. Dept. of Commerce NOAA–NWS Climate Analysis Center, 90 pp.
- Hartmann, D. L., M. E. Ockert-Bell, and M. L. Michelsen, 1992: The effect of cloud type on the Earth's energy balance: Global analysis. *J. Climate*, **5**, 1281–1304.
- Jin, Y., and W. B. Rossow, 1994: Investigation and Comparison of ISCCP and HIRS high level clouds. *Eighth Conf. on Atmospheric Radiation*, Nashville, TN, Amer. Meteor. Soc., 64–65.
- Kousky, V. E., 1992: Near real time analysis ocean/atmosphere for January 1992. NOAA Climate Diagnostics Bulletin No. 92/1, 90 pp.
- McCleese, D. J., and L. S. Wilson, 1976: Cloud top height from temperature sounding instruments. *Quart. J. Roy. Meteor. Soc.*, **102**, 781–790.
- Menzel, W. P., and K. I. Strabala, 1989: Preliminary report on the demonstration of the VAS CO₂ cloud parameters (cover, height, and amount) in support of the Automated Surface Observing System (ASOS). NOAA Tech. Memo. NESDIS 29, 19 pp.
- , W. L. Smith, and T. R. Stewart, 1983: Improved cloud motion wind vector and altitude assignment using VAS. *J. Climate Appl. Meteor.*, **22**, 377–384.
- , D. P. Wylie, and A. H.-L. Huang, 1986: Cloud top pressures and amounts using HIRS CO₂ channel radiances. *Tech. Proc. Third Int. TOVS Study Conf.*, Madison, WI, NOAA, 173–185.
- , —, and K. I. Strabala, 1989: Characteristics of global cloud cover derived from multispectral HIRS observations. *Tech. Proc. Fifth Int. TOVS Study Conf.*, Toulouse, France, NOAA, 276–290.
- , —, and —, 1992: Seasonal and diurnal changes in cirrus clouds as seen in four years of observations with the VAS. *J. Appl. Meteor.*, **31**, 370–385.
- Minnis, P., E. F. Harrison, L. L. Stowe, G. G. Gibson, F. M. Denn, D. R. Doeling, and W. L. Smith Jr., 1993: Radiative climate forcing by the Mount Pinatubo eruption. *Science*, **259**, 1411–1415.
- Rossow, W. B., and A. A. Lacis, 1990: Global and seasonal cloud variations from satellite radiance measurements. Part II: Cloud properties and radiative effects. *J. Climate*, **3**, 1204–1253.
- Sassen, K., 1992: Evidence of liquid phase cirrus cloud formation from volcanic aerosols: Climatic implications. *Science*, **257**, 516–519.
- Smith, W. L., and C. M. R. Platt, 1978: Intercomparison of radio-sonde, ground based laser, and satellite deduced cloud heights. *J. Appl. Meteor.*, **17**, 1796–1802.
- , H. M. Woolf, P. G. Abel, C. M. Hayden, M. Chalfant, and N. Grody, 1974: Nimbus 5 sounder data processing system. Part I: Measurement characteristics and data reduction procedures. NOAA Tech. Memo. NESS 57, 99 pp.
- Stowe, L. L., G. G. Wellemeier, T. F. Eck, H. Y. M. Yeh, and the Nimbus-7 Cloud Data Processing Team, 1988: *Nimbus-7 global cloud climatology. Part I: Algorithms and validation*. *J. Climate*, **1**, 445–470.
- , R. M. Carey, and P. Pellegrino, 1992: Monitoring the Mt. Pinatubo aerosol layer with NOAA/11 AVHRR data. *Geophys. Res. Lett.*, **19**, 159–162.
- Susskind, J., D. Reuter, and M. T. Chahine, 1987: Cloud fields retrieved from analysis of HIRS/MSU sounding data. *J. Geophys. Res.*, **92**, 4035–4050.
- Warren, S. G., C. J. Hahn, J. London, R. M. Chervin, and R. L. Jenne, 1988: Global distribution of total cloud over and cloud type amounts over the ocean. NCAR Tech. Note NCAR/TN-317+STR, 212 pp. [Available from the National Center for Atmospheric Research, Boulder, CO, 80307.]
- Weare, B. C., 1992: Variations in Nimbus-7 cloud estimates. Part I: Zonal averages. *J. Climate*, **5**, 1496–1505.
- Wielicki, B. A., and J. A. Coakley, 1981: Cloud retrieval using infrared sounder data: Error analysis. *J. Appl. Meteor.*, **20**, 157–169.
- , and Parker, 1992: On the determination of cloud cover from satellite sensors: The effect of sensor spatial resolution. *J. Geophys. Res.*, **97**, 12 799–12 823.
- Wu, M. L., and J. Susskind, 1990: Outgoing longwave radiation computed from HIRS2/MSU soundings. *J. Geophys. Res.*, **95D**, 7579–7602.
- Wylie, D. P., and W. P. Menzel, 1989: Two years of cloud cover statistics using VAS. *J. Climate Appl. Meteor.*, **2**, 380–392.
- , and —, 1991: Two years of global cirrus cloud statistics using HIRS. *Tech. Proc. Sixth Int. TOVS Study Conf.*, Airlie, VA, NOAA, 344–353.

Appendix B

UNDERSTANDING SATELLITE CIRRUS CLOUD CLIMATOLOGIES WITH
CALIBRATED LIDAR OPTICAL DEPTHS

Donald Wylie and Paivi Piironen
Space Science and Engineering Center
University of Wisconsin-Madison
Madison, WI 53706

Walter Wolf and Edwin Eloranta
Department of Atmospheric and Ocean Sciences
University of Wisconsin-Madison
Madison, WI 53706

To be published in the Journal of Atmospheric Sciences

July 1994

Revised January 1995

Abstract

Optical depth measurements of transmissive cirrus clouds were made using coincident lidar and satellite data to improve our interpretation of satellite cloud climatologies. The University of Wisconsin High Spectral Resolution Lidar was used to measure the optical depth of clouds at a wavelength of 532 nm while the GOES and AVHRR window channel imagers provided measurements at a wavelength of 10.8 microns. In single layer cirrus clouds with a visible optical depth greater than 0.3, the ratio of the visible to the IR optical depth was consistent with the approximate 2:1 ratio expected in clouds comprised of large ice crystals.

For clouds with visible optical depths < 0.3 , the Visible/IR ratios were nearly always < 2 . It is likely that this reflects a measurement bias rather than a difference in cloud properties.

Most cirrus clouds observed in this study were more than 1 km thick and were often comprised of multiple layers. Super cooled liquid water layers coexisted with the cirrus in 32% of the cases examined. In many of these cases the presence of water was not evident from the satellite images. Thus, it must be concluded, that "cirrus" climatologies contain significant contributions from coexisting scattered and/or optically thin water cloud elements.

1. INTRODUCTION

Predictions of global warming from the increase of CO₂ in the atmosphere have lacked credibility due to the need to assess the contribution of clouds to the radiation budget (Stephens, 1994, Liou, 1980, and Paltridge, 1980). Cirrus clouds, in particular, have the ability to either offset the CO₂ warming or contribute to tropospheric warming through interaction with solar and terrestrial radiation passing through the clouds. Thin partially transmissive cirrus in the upper troposphere can add to tropospheric warming by transmitting solar radiation while capturing terrestrial radiation from below and re-radiating to space at a colder temperature. Thick cirrus and multiple layer cirrus, where water clouds are present under the cirrus, produce highly reflective cloud combinations that can raise the albedo and reduce the solar insolation. Predictions of climate changes must ultimately include the effects of these clouds on radiative transfer processes. However, Stephens et al. (1990) point out that the effect of clouds on the earth's radiation budget is not understood because of the lack of data.

Global cloud and radiation data sets are presently being collected from satellites. The International Satellite Cloud Climatology Project (ISCCP, Schiffer and Rossow, 1983, and Rossow and Schiffer, 1991) has measured cloud cover and radiation for 11 years using the operational weather satellites. Wylie et al. (1994) have studied cirrus clouds from four years of NOAA polar orbiting satellite data, also Woodbury and McCormick (1983) have made a similar analysis of global cirrus from the SAGE II data on the NIMBUS-7 satellite.

Inter-annual changes in cloud cover have been found. The Wylie et al. (1994) study reported an increase in cirrus with the recent El Nino-Southern Oscillation (ENSO) that began in 1991. A similar change in cloud cover in the 1982-83 ENSO was also found by Weare (1992) using the NIMBUS 7 data set. These studies indicate that cloud cover is linked to climatic fluctuations.

Estimates have been made of the effect of lower tropospheric clouds on the earth's heat budget by Tselioudis et al. (1992) using ISCCP data, but similar calculations for upper tropospheric clouds have not been attempted because of the complications of estimating the

effects of both the visible and infrared radiative processes together. Cirrus clouds affect both infrared and solar radiative transfer through the atmosphere while the lower tropospheric clouds studied by Tselioudis et al. (1992) affect mainly solar radiation.

The satellite cloud climatologies have been restricted to either visible or infrared data. Wylie et al. (1994) and Weare (1992) used longwave infrared data while the ISCCP used visible sensors for detecting transmissive clouds. Infrared data is also used by the ISCCP to detect non-transmissive clouds and assign cloud heights, but the radiative properties of cirrus are calculated from the visible data. None of these climatologies have calculated the visible and infrared properties of clouds simultaneously.

The satellite cloud climatologies also are constrained to reporting only one level for the clouds and do not define the vertical depth of the clouds, the vertical profile of visible extinction, or infrared absorption. Attempts have been made to identify multiple cloud levels from satellite data. However, these algorithms require a priori knowledge of the vertical profile of the cloud to obtain unique solutions. The single value representing the cloud level is the only unique solution that can be obtained without information in addition to the satellite radiance observations. In very dense clouds, the cloud level derived from the satellite data is very close to the cloud top. For partially transmissive clouds, a lower level is given.

To use the global cloud climatologies produced from satellite data, we need to understand how they represent complicated cloud forms. We know that complicated situations with multiple level clouds are very common. A comparison of satellite cloud retrievals to ground based National Weather Service observations over the continental United States found that low and middle tropospheric clouds were present in 52% of the cases where the satellite cloud detection system found an upper tropospheric cloud (Menzel et al., 1992). Similar frequencies of multiple cloud layers over oceans are shown in Hahn et al. (1982). Lidar data collected at the University of Wisconsin-Madison (Figure 1) found that cirrus are often geometrically thick reaching depths up to 5 km. Thus, we expect that cirrus are more complicated than the assumed thin single layer model used in the cloud retrieval algorithms.

Because of the uncertainty of what satellite cloud retrievals represent, we collected a data set of high quality lidar observations with coincident satellite data. The purpose of this study is to assess the applicability of the single cloud height and optical depth derived by one satellite cloud climatology and evaluate how this information should be used. The cloud analysis method examined here will be the one used in the climatology of Wylie et al. (1994) called the CO2 Slicing Method. This climatology uses multispectral infrared data from 10.8 to 15 microns wavelength. A cloud level is calculated from the 13 to 15 micron measurements of the High Resolution Infrared Radiometer Sounder (HIRS) on the NOAA polar orbiting satellites. An optical depth at 10.8 microns in the infrared also is derived from the same satellite data. This study compared satellite derived infrared optical depths to the visible wavelength optical depths and vertical profiles of extinction derived from a ground based lidar.

2. MEASUREMENT TECHNIQUE

This study was initiated in 1989 using the unique measurement systems at the University of Wisconsin-Madison (Ackerman, et al., 1993). Visible optical depths of cirrus were obtained from the High Spectral Resolution Lidar (HSRL) while infrared optical depths were obtained from satellite data so that the information collected could be related to the cirrus climatology of Wylie et al. (1994).

2.a. The HSRL

In order to make reliable measurements of the extinction profile, the HSRL measures two signals from the 0.532 μm transmitted pulse which can be processed to yield separate lidar returns for aerosol and molecular scattering. This separation is possible because the spectrum of the molecular lidar return is Doppler broadened by the thermal motion of the molecules while the slow moving aerosol particles generate negligible spectral broadening. The molecular scattering cross section is a function of molecular density and can be calculated from Raleigh scattering theory and an independently measured temperature profile. The HSRL then uses molecular scattering as a calibration target which is available at each point in the lidar return.

Two lidar returns are derived; these are given by the following equations for the signal power received from molecular scattering, $P_m(r)$, and aerosol scattering, $P_a(r)$:

$$P_m(r) = E_o \frac{cA_r}{2r^2} \beta_m(r) \frac{3}{8\pi} \exp(-2\tau(r)) \quad (1)$$

$$P_a(r) = E_o \frac{cA_r}{2r^2} \beta_a(r) \frac{P(\pi,r)}{4\pi} \exp(-2\tau(r)) \quad (2)$$

E_o = Laser pulse energy, J.

c = Speed of light, ms^{-1} .

A_r = Collecting area of the receiver, m^2 .

r = Range to the scattering volume, m.

β_a = Aerosol scattering cross section per unit volume, m^{-1} .

β_m = Scattering cross section per unit volume for air molecules, m^{-1} .

$\frac{P(\pi,r)}{4\pi}$ = Aerosol backscatter phase function, sr^{-1} .

τ = Optical depth.

Equation 1 contains two unknowns: the optical depth between the lidar and the scattering volume, $\tau(r)$, and the molecular scattering cross section, $\beta_m(r)$. Molecular scattering is described by the Rayleigh scattering equation and is directly proportional to atmospheric density, $\rho(r)$.

$$\beta_m(r) = C\rho(r)$$

Thus if we define a range-squared, energy corrected molecular lidar return:

$$S_m(r) = P_m(r)r^2/E_o$$

$$\ln[S_m(r)] = \text{constant} + \ln[\rho(r)] - 2\tau(r)$$

The optical depth between any two ranges, r and r_o , is given by:

$$\tau(r) - \tau(r_o) = 0.5 \ln[\rho(r)/\rho(r_o)] - 0.5 \ln[S_m(r)/S_m(r_o)] \quad (3)$$

The average extinction cross section in a layer between r_o and r can be computed from equation 3:

$$\overline{\beta_e(r,r_o)} = [\tau(r) - \tau(r_o)]/[r-r_o] \quad (4)$$

More details can be found in Grund and Eloranta (1991) and Piironen and Eloranta (1994).

2.b. Satellite Infrared Data Analysis

The satellite cloud analysis of Wylie et al. (1994) assumes that the radiative effects of the clouds occur at only one level in the troposphere. This allows a simple calculation of cloud

emittance at 10.8 μm , the longwave window channel, from the radiances measured by the satellite in the cloudy pixel (R_{sat}), a clear pixel (R_{clr}), and the radiance expected if an opaque cloud were present at the pixel (R_{cld}).

$$\epsilon_{11} = [R_{\text{clr}} - R_{\text{sat}}] / [R_{\text{clr}} - R_{\text{cld}}] \quad (5)$$

R_{sat} was measured from the pixel over the HSRL while R_{clr} is an estimate of the radiance that would have been measured if the cloud was not present. This clear radiance estimate was derived from the nearest clear pixel by assuming that the background under the cloud was the same as at the location where R_{clr} was taken. R_{cld} was calculated from the temperature of the mid-cloud level using rawinsonde data from the two closest National Weather Service stations, Green Bay, WI, 175 km to the northeast and Peoria, IL, 225 km to the south.

To simplify the calculation, the equivalent blackbody temperature to the fourth power (T^4) was used in place of R . The equivalent blackbody temperature was calculated from the measured radiances using the sensor channel spectral response filter functions. The satellite measurements are calibrated to both radiance (R) and equivalent blackbody temperature (T). Equation 5 can be expressed as:

$$\epsilon_{11} = [T_{\text{clr}}^4 - T_{\text{sat}}^4] / [T_{\text{clr}}^4 - T_{\text{cld}}^4] \quad (6)$$

where:

- T_{clr} = blackbody brightness temperature for a clear pixel
- T_{sat} = equivalent blackbody brightness temperature for a cloudy pixel
- T_{cld} = the air temperature at the mid-cloud height.

The mid-cloud altitude was determined from the HSRL backscatter vertical profile. This approximated the cloud level that the HIRS CO2 Slicing analysis reports for transmissive clouds (Wylie and Menzel, 1989).

The emittance (ϵ_{11}) calculated by (6) will be larger than absorption emittance because we have not accounted for scattering into the field of view of the sensor. Scattered radiation could raise the calculated value of ϵ_{11} by ≈ 0.1 over the true absorption emittance according to the model of Platt and Stephens (1980). Moderately transmissive clouds ($\epsilon \approx 0.50$) are affected the most by

scattering, while very thin ($\epsilon \approx 0.00$) and very dense clouds ($\epsilon \approx 1.00$) will have little error from scattered radiation.

IR optical depths at 10.8 microns were calculated from the emittances by assuming that transmission is the complement of emission without scattering:

$$\tau_{ir} = -\ln(1 - \epsilon_{11}) \quad (7)$$

The infrared optical depths were corrected for the angle of the satellite view using the cosine of the zenith angle.

3. DATA

HSRL data were examined for 48 days covering all four seasons. Comparisons were made to satellite data on 19 days (see Table 1). NOAA-12 overpasses of Madison, WI were available when most of the HSRL data were taken. However, on six days, GOES 7 data were used because of the absence of NOAA-12 data. The comparisons were restricted to cases with visible optical depths < 3 when the HSRL probed through the entire cloud. Total cloud penetration was determined by the presence of molecular backscatter signal beyond the cloud top (Equation 1).

4. RESULTS

4.a. Visible and IR Optical Depths

To compare visible and infrared radiative properties, satellite infrared optical depths from Equation 7 were plotted with the HSRL visible optical depths from Equation 3 (see Figure 2). The 19 cases covered a variety of transmissive cirrus situations. The clouds were separated into three classes; geometrically thin single layers, < 2.5 km altitude, geometrically thick single layers, > 2.5 km altitude, and multi-layered clouds. Many of the multiple level cloud cases included a thin layer of super cooled liquid water (distinguished by low values of depolarization measured by the HSRL) and often included ice crystals precipitating from the layer. Liquid water layers embedded in cirrus were found on 32% of the 48 days that the HSRL collected cirrus data. Liquid water also was present on 6 of the 19 days compared to satellite data (see Table 1).

Error estimates for both the HSRL and satellite optical depth measurements are also included in Figure 2. For the visible optical depth (horizontal bars) the error was computed from an analysis including photon counting statistics, error in the observed density profile, and error in system calibration. For the satellite infrared optical depths (vertical bars), the error was estimated by assuming a 2 K error in each variable in Equation 6. This is our estimate of the maximum uncertainty in determining the clear equivalent blackbody temperature (T_{clr}) and the cloud temperature (T_{cld}). The largest sources of clear radiance errors were spatial gradients in the land surface, low level aerosol gradients and water vapor gradients between the location of the HSRL and where T_{clr} was obtained. The largest source of T_{cld} error was the air temperature gradient between the location of the HSRL and the rawinsonding. The satellite radiometric measurements are calibrated to 0.8 K which is a far better accuracy than the other error sources. The location of the HSRL in the satellite images was also determined to an accuracy of < 1 pixel using navigation adjustments from rivers and lake shorelines.

4.b. Single Layer Cirrus

An example of a single layer cirrus cloud is shown in Figure 3 from 26 October 1993. The cirrus cloud was found to be between heights of 9 and 11 km and was fairly uniform in the vertical dimension and in time as seen in the lidar time section. The NOAA satellite image (Figure 4) showed very uniform conditions around the HSRL (black dot on the image). Brightness variations in the satellite image around the HSRL span a range of only 2 K in equivalent blackbody temperature. The visible optical depth was 0.5 at the time of the NOAA overpass (0:30 UT). The satellite infrared optical depth was found to be 0.28, yielding a $\tau_{\text{vis}}/\tau_{\text{ir}}$ ratio of 1.8.

The IR optical depth, τ_{ir} , may have been over estimated because we assumed the low level aerosol layer from 0-3.2 km altitude found by the HSRL (Fig. 3) was present where T_{clr} was measured 150 km to the southeast on the satellite image (Fig. 4). The cirrus over the HSRL was part of a large air mass moving from the southwest to the northeast. This air mass did not cross the HSRL so we did not measure the aerosol optical depth in it. We assumed its presence because

of the reduction of spatial detail of land features in this area from other images. If the low level aerosol and accompanying water vapor were not present where T_{clr} was measured, then τ_{ir} was over estimated.

4.c. The Effects of Multiple Cloud Layers

Multiple layers of clouds were very common during this study. Six cases of multiple layered clouds were examined. One example is shown in Figure 5 for 11 November, 1993 when the cirrus was changing during the HSRL observation. Initially, only one layer of cirrus from 7 to 10 km was present; then at 1:15 UT a second layer appeared. Depolarization measurements by the HSRL indicated that the intense backscatter levels (solid white) were liquid water particles while the rest of the cloud was ice. Visible optical depths were from 0.4-0.6 in the upper layer. The optical depths increased to 1.0 at the NOAA overpass at 1:30 UT because of the addition of the lower cloud layer. After 1:40 UT the visible optical depth exceeded 3.0, the maximum measurable by the HSRL.

The NOAA-12 IR image in Figure 6 also shows this change as cold and dense clouds moved in from the west. Striations in the satellite image indicate the possible existence of two cloud layers. To the east (down wind) a northwest-southeast pattern of striations is faintly visible in Figure 6. While the colder area to the west (up wind) has a southwest-northeast striation pattern orthogonal to the pattern east of the HSRL. Both patterns are skewed to the westerly wind. Our first impression of this image was that the cloud field changed from low to high clouds, while the HSRL data revealed an opposite change from a single continuous high cloud layer to the addition of a second lower cloud layer.

The liquid water layer dominated the optical depth of the combined cirrus layers after 1:30 UT on the HSRL. The upper ice cloud maintained a nearly constant optical depth of 0.4-0.6 until 01:40 UT when the HSRL could no longer penetrate through the water layer.

The satellite measured equivalent blackbody temperature decreased from 262 K before the lower layer formed (to the east in the image), to 253 K at the HSRL location. In the dense two

layer cloud it dropped to 243 K at 30 km west of the HSRL in the image. At 01:00 UT on 11 November when the single cirrus layer was present at a mean height of 8.5 km, the infrared optical depth calculated from Equations 5 and 6 was 0.25 using $T_{\text{sat}} = 262$ K.

The response of the multi-spectral HIRS algorithm to the cloud structures observed by the HSRL was simulated for the satellite over pass at 01:30 UT, 11 November, 1993 and when the lower water layer first obscured the HSRL at 1:40 UT. The simulations calculated what the HIRS channels would have seen given the temperature structure and the infrared emittance and transmittance of each cloud layer. HIRS data were not available at the location of the HSRL. The HIRS pixels do not overlap and contain gaps between pixels that are about the same dimensions as the Field Of View (FOV) of the HIRS channels. For accurate comparisons to the HSRL, radiative data must come from the location of the HSRL. Spatial variance of the clouds can cause large errors. These errors are discussed in detail in section 4d.

The radiance received by each HIRS channel was estimated using a simple model of two non-scattering cloud layers.

$$I_i = \int_{p_1}^0 B[i, T(p)] \{dS_i(p)/dp\} dp + S_i(p_1) \epsilon_1 B[i, T(p_1)] \quad (8)$$

$$+ (1 - \epsilon_1) \left[\int_{p_2}^{p_1} B[i, T(p)] \{dS_i(p)/dp\} dp + S_i(p_2) \epsilon_2 B[i, T(p_2)] \right]$$

$$+ (1 - \epsilon_1)(1 - \epsilon_2) \left[\int_{p_{\text{sfc}}}^{p_2} B[i, T(p)] \{dS_i(p)/dp\} dp + S_i(p_{\text{sfc}}) B[i, T(p_{\text{sfc}})] \right]$$

Where:

$B[i, T(p)]$ = the Planck function for spectral channel (i) and temperature $T(p)$,
 $S_i(p)$ = the transmittance of the radiation from pressure level p through the top of the atmosphere and
 ϵ_x = the emittance for cloud layer x .

The emittance (ϵ) for each cloud layer was approximated from the HSRL measurements of the visible optical depth of the layer. The infrared optical depth was assumed to be one half of the visible optical depth for each cloud layer and the emittance (ϵ) was derived from Equation 7.

The approximated radiances for the HIRS channels were used in the algorithm described by Wylie et al. (1994) for determining a single cloud level. This cloud level was then used to obtain

T_{cld} from the rawinsonde data. With a new T_{cld} and the measured T_{sat} and T_{clr} , Equations 6 and 7 were re-applied to give an estimate of what the HIRS algorithm would have derived for the cloud altitude and infrared optical depth (τ_{ir}). Note that this calculation used a combination of satellite measured equivalent blackbody temperatures, T_{sat} and T_{clr} and a new temperature for the approximate single cloud level, T_{cld} .

The two cloud layers observed at 01:30 and 01:40 UT, presented a problem to the basic assumption used in satellite cloud retrievals - the single level description of the cloud. The expected response of the multi-spectral HIRS CO2 Slicing cloud retrieval algorithm used by Wylie et al. (1994) to multi-layered clouds is that it would place the single cloud height between the two layers (Wielicki and Coakley, 1981 and Menzel et al., 1992). When one cloud layer has greater optical depth than the other, the multi-spectral HIRS CO2 Slicing cloud height solution is expected to move toward the denser layer. An exception to this trend occurs when the top layer is nearly opaque and obscures the view of the lower layer, forcing the CO2 Slicing solution into the top layer.

Attempts have been made to extract more than one cloud level from the multi-spectral HIRS data. However, the solution of the radiative transfer model for the HIRS channels requires the integral of the radiation over a broad depth of the troposphere. Altitude sensitivities of the channels are broad and overlap. Each HIRS channel receives radiation from 3-5 km of the troposphere. To solve for more than one cloud level, the vertical profile of the clouds must be determined. Since each HIRS channel sees the integral of the radiation over a large depth of the troposphere, a wide variety of cloud structures could be present from which no unique solution can be made. The only tractable solution for the HIRS data is one cloud level.

At 1:30 UT the HIRS radiances were calculated from Equation 8 using two cloud levels at 5 and 8.5 km. The visible optical depth of each layer measured by the HSRL was 0.5 totalling 1.0 for the combination. Infrared emittances were calculated to be 0.22 for each layer by assuming that the infrared optical depths were one half of the visible HSRL measurements and using Equation 7 to derive emittances. A single cloud height of 7.1 km was calculated from the CO2

Slicing algorithm (Wylie et al., 1994) using the radiances calculated by Equation 8. This estimate of the cloud height is between the two cloud layers. The infrared optical depth calculated from 7.1 km cloud height and the AVHRR measured $T_{\text{sat}} = 253$ K, was 0.8.

At 1:40 UT when the total optical depth reached the maximum observable by the HSRL, Equation 8 was employed to estimate HIRS radiances. The upper cloud layer remained at the same optical depth as measured at 1:30 UT (0.5) and the lower cloud layer was 3.0. The CO2 Slicing single cloud level solution was 6.5 km, lower than calculated at 1:30 UT.

This is an example of how the HIRS CO2 Slicing single cloud level solution used by Wylie et al. (1994) responds to multiple level clouds. The technique is constrained to reporting only one cloud layer. For one layer of transmissive cirrus, it places the cloud level near the center of the layer as predicted by Wielicki and Coakley (1981). Similar results for a previous comparison with lidar data were reported in Wylie and Menzel (1989). For two layers, the HIRS solution was between the layers, but displaced toward the denser layer.

4.d. The Effects of Vertical and Horizontal Variability

Most of the variations in the optical depths came from horizontal variations in the cirrus clouds. An example on 2 September, 1993 is shown in Figure 7. The NOAA-12 satellite image from the 01:36 UT overpass (Figure 8) shows a small and narrow cirrus cloud which is partially over the HSRL (dot in the image). This cloud moved east on a 75° heading. Only part of it crossed the HSRL. Larger clouds up wind crossed the HSRL at 01:55 UT. This is an example of how spatial variability affected the lidar-satellite comparison. The visible optical depth at the time of the satellite overpass was 0.2 while the infrared optical depth at the presumed HSRL location was 0.05 yielding $\tau_{\text{vis}}/\tau_{\text{ir}} = 4$, larger than expected. The satellite equivalent blackbody temperature was taken in a gradient region where any error in location could raise or lower its value. Also, for horizontally small and narrow clouds, the larger size of the satellite radiometer's FOV may have averaged more cloud area with less cloud optical depth than that viewed by the HSRL.

Another example of a variable cloud situation was found on 15 April, 1994 (see Figures 9 and 10). The HSRL image of backscatter cross section (Figure 9) showed large variations in the optical depth with time while the NOAA-12 AVHRR image (Figure 10) showed cirrus clouds with a variety of shapes. An elongated cloud partially covered the HSRL at the time of the satellite overpass (00:49 UT) and moved toward the northeast on a 80° heading. There were at least two layers of cirrus as indicated in Figure 9. The lower layer was more dense but highly variable in nature and contained some super cooled water. The upper layer was very thin and composed entirely of ice. The visible optical depth was 0.75 while the infrared was 1.07, higher than expected ($\tau_{\text{vis}}/\tau_{\text{ir}} = 0.7$).

To statistically estimate the errors of FOV size differences and possible miss-registration of the satellite image, data from the Volume Imaging Lidar (VIL) were examined. This is a 1064 nm Nd:YAG lidar with an optics system that scans from horizon to horizon. It was operated on 1 December, 1989 for two hours when transmissive cirrus were present. The VIL performed a pair of scans in 2 minute cycles. The cycle consisted of an across the wind scan (north to south) followed by an along the wind scan (east to west). Examples of images made from these scans are shown in Figures 11 and 12. The cross wind scans are the upper panel and the along wind scans are the lower panel.

The two hour period from 19:30 to 21:30 UT (13:30 to 15:30 CST) began with light broken cirrus to the north and one line of precipitating cirrus to the south (see Fig. 11). The cirrus to the north were in small patches at a variety of levels from 6.5 to 9 km in altitude. Light virga were observed. One large contrail appeared at 7.7 to 8.5 km altitude, 15 km south of the VIL (center point). A dense line of precipitating cirrus was also found 30 to 43 km south of the VIL. About 75 minutes later dense cirrus moved over the VIL (Fig. 12). A nearly continuous cloud from 6.5 to 9.3 km altitude was present within most of the range of the VIL. Some optically dense layers were found at 7 and 9 km.

To quantify the effects of cloud spatial variability on scanning method and FOV size, the backscatter measured by the VIL was vertically integrated from the series of slant angle scans in

each cross section. Although the backscatter to extinction relationship may not be simple, we can assume that the backscatter is nearly linearly related to extinction for these optically thin clouds. The vertical integral of backscatter through the cloud is proportional to the optical depth of the cloud when the optical depth is small. The effect of this simplification is that the optical depth structural variations are most likely larger than the backscatter structural variations that are shown in Figures 13 and 14.

The cross wind scans were used to describe the areal structure of the cloud. Wind advection through each scan implied that the clouds were sampled at approximately 3 km intervals. Since the VIL cross sections have 100 m resolution along the scan, the cloud volume was sampled with a resolution of 0.1×3 km.

To estimate the effects of cloud structural variance on the averaged vertically integrated backscatter, two spatial averages were made. One average was obtained from the cross wind scans using wind advection to represent the satellite's spatial sampling. The other average was obtained from the along wind scans to represent the sampling of a vertically pointing lidar that uses wind advection for cloud sampling. Each average was constructed for simulated satellite FOV diameters of 1, 4, 8 and 20 km. The along wind scans have only the width of the lidar beam (< 1 m) and thus the average is a line sample. The difference between these two averages of vertically integrated backscatter was used to approximate the sampling error between the satellite and stationary lidar sensors. This error is expressed as a fraction of the along wind lidar average in Figures 13 and 14. To estimate the possible error from mis-registration of the satellite image, the cross wind sampled segment was shifted from the center position of the VIL, see Figures 13 and 14.

The error between line and areal averaged measurements at 0.0 km displacement ranged from 5 to 29% (left most point in Figures 13 and 14). It was higher for the light and scattered cirrus simulating a 20 km FOV (Figs. 11 and 13) than the smaller simulated FOVs and the denser cirrus (Figs. 12 and 14). In the denser cirrus, the line vs. area sampling error ranged from 20 to 25 % (Fig 14).

The misalignment test shows that the area-line error increases with cross wind misalignment. The light cirrus (Fig. 13) have very large errors because of the spacing between cirrus features of 12-20 km and close alignment of the structures with the direction of the wind. The error or difference from the cross wind average often exceeded the along wind average (error > 100 %). These errors were smaller in the denser cirrus (Fig. 14). Operational satellites often have image registration errors of 12 to 20 km. A 12 km misalignment when compared to a ground based sensor can cause an error of 50 % or greater. For larger FOV sizes of 8 and 20 km, this error decreases slightly. Because of this problem, special effort was made to align the satellite images to a one pixel accuracy. Methods for making alignment corrections are described in Krasnopolsky and Breaker (1994).

5. DISCUSSION

For the six single layer cloud cases where visible optical depths exceeded 0.3 and infrared optical depths exceeded 0.15, an average $\tau_{\text{vis}}/\tau_{\text{ir}}$ of 2.06 was found. The error analysis shown by the error bars in Figure 2 imply a possible measurement error of ± 0.77 in this ratio for individual cases. The error of the mean ratio of the six cases is ± 0.36 . Other studies by Platt (1979), Platt et al. (1987) and Minnis et al. (1990) have found similar relationships from simultaneous measurements of the visible and infrared properties of cirrus clouds.

More variability in the lidar-satellite comparison ($\tau_{\text{vis}}/\tau_{\text{ir}}$, Fig. 2) was found in multiple layered clouds and optically thin clouds. The major problem was differing methods of scanning the clouds between the lidar and satellite sensors. The high spatial variability of the clouds affected each sensors representation of the clouds. The Volume Imaging Lidar showed that the thin line sampling of the HSRL vs. the areal scan of the satellite sensors could cause differences of 20-25% in measurements of the same variable. Any mis-registration of the location of the HSRL in the satellite image caused potentially larger errors and had to be corrected in this study. The initial evaluation of the HSRL and satellite data had more scatter than shown in Figure 2. This gave the impression that variations in cloud structure and microphysical content were causing variations in

the visible-infrared optical depth relationship. Re-analysis of the data with an intensive effort to remove location uncertainties reduced the scatter in Figure 2.

The satellite measurement of τ_{ir} for optically thin clouds ($\tau_{vis} < 0.3$) also had a bias because of the way in which the numerator of Equation 6 ($T_{clr}^4 - T_{sat}^4$) was evaluated. This required a measurement of the difference between the clear and cloudy equivalent blackbody temperatures in the satellite image. For optically thin clouds, variations in the underlying land surface were of nearly the same magnitude as ($T_{clr} - T_{sat}$). The precision and noise characteristics of the satellite sensors require that the numerator terms in Equation 6 be at least 0.8 K different ($T_{clr} - T_{sat} > 0.8K$) for the cloud to be distinguished on the satellite image. Variations in the background under the cloud cause even larger variations in the measured equivalent blackbody temperatures. Other blackbody temperature variations come from variability in the clouds, as previously discussed, and the possibility of the cloud covering only part of the sensor's FOV. Because of these problems, we required $T_{clr} - T_{sat} > 2$ K before calculating τ_{ir} . Any smaller blackbody temperature differences ($T_{clr} - T_{sat} < 2$ K) were considered to be below our cloud detection limit. This detection limit is similar to the quality control editor used by Wylie et al. (1994). Wylie and Menzel (1989) estimated that 50% of the cirrus clouds with $\tau_{ir} \approx 0.1$ ($\tau_{vis} \approx 0.2$) are not detected in their satellite data. This forced a minimum value of τ_{ir} from 0.04 to 0.1, depending on the level and temperature of the cloud. The result of editing for cloud detection errors, is that the detected clouds have a non-random error and are biased toward larger τ_{ir} .

In this study we knew that cirrus were present from the HSRL data so we had to find a T_{clr} to solve Equation 6. T_{clr} may have been selected from a warmer location than the HSRL to fulfill the $T_{clr} - T_{sat} \geq 2$ K requirement. This would have biased τ_{ir} upward explaining why 7 of the 9 points in Figure 2 with $\tau_{vis} < 0.3$ have τ_{vis}/τ_{ir} ratios < 2 (above the line).

Cirrus with $\tau_{vis} > 0.3$ best conformed to the single cloud level assumption made by most satellite cirrus cloud detection algorithms even though they span depths of 1-3 km. Dense cirrus with optical depths $\tau_{vis} > 1$ ($\tau_{ir} > 0.5$), were found to be over 3 km thick and in two or more layers.

Vertical variations in optical density were common and liquid water layers were often present inside the ice clouds.

The retrieval of a single cloud level from the HIRS data is useful for approximating radiative properties of transmissive clouds. More detail in the vertical would be helpful for the development of radiative transfer models. But the satellite data are currently limited to one level solutions of transmissive clouds. Satellite data have to be used to study transmissive clouds globally and monitor their variations, seasonally and inter-annually. No other data source can provide global coverage at this time.

The cloud altitude calculated from the satellite data is more useful than the cloud top height by itself. The original intent of the CO₂ Slicing algorithm was to find the height of the cloud top. The calculated cloud level is more useful because it can be used with the radiances measured by the satellite to calculate cloud radiative properties. This can be done only for clouds in which infrared transmission is detected in the satellite data and cannot be done for clouds opaque to infrared radiation. However, infrared transmissive clouds cover from 35-40% of the earth (Wylie et al., 1994) and are a significant component in the earth's heat budget.

The presence of super cooled liquid water layers in 32% of the 48 days of HSRL data which was more frequent than we expected. (This 48 day sample includes 29 days which were not compared to satellite data.) The HSRL was operated mostly during NOAA-12 overpasses at dusk and after dark when cirrus clouds were apparent from visual observations of the sky. Lower water clouds were not present when these data were taken. Thus the presence of liquid water embedded in the ice clouds was not anticipated by the HSRL operators.

6. SUMMARY AND CONCLUSIONS

Statistics on the frequency, altitude and optical depths of cirrus clouds obtained from satellite multi-spectral infrared data (the HIRS) are representative of the general properties of these clouds in spite of the limitations of cloud analysis algorithm. The algorithm used by Wylie et al. (1994) on multi-spectral HIRS data assumed that all the radiative properties of the cloud

occurred at one level in the vertical. Cirrus clouds are seldom found as one thin vertical layer, but are thick and often comprised of two or more layers. In spite of the limitation of the one cloud level assumption, the single cloud level and infrared optical depth derived from the satellite data were indicative of the bulk characteristics of thick cirrus. The cloud level reported was closer to the center of the cloud or layers of cloud rather than the cloud top. The infrared optical depth was close to the optical depth of the combination of all the layers except for optically thin cirrus where infrared optical depths tend to be over estimated.

Differences between the lidar and satellite measurements of optical depths were mostly caused by the differences in the method of scanning the clouds and the horizontal variability of these clouds. Cirrus clouds are highly variant spatially in optical density. Large differences in the optical depth measurements resulted from the sensors seeing different portions of the clouds.

Most cirrus clouds observed in this study were more than 1 km thick and often comprised of multiple layers. Super cooled liquid water layers coexisted with the cirrus in 32% of the cases examined. In many of these cases the presence of water was not evident from the satellite images. Thus, it must be expected that "cirrus" climatologies contain significant contributions from coexisting scattered and/or thin water cloud elements.

Cirrus clouds exhibit spatial structure on a wide range of scales. This structure is different in the along-the-wind and cross-wind directions. This spatial structure implies that time averages of vertical profiles above a point may not provide good estimates of the spatially averaged quantities derived from satellite data. This provides a significant source of error in comparisons of non-scanning lidar data with satellite observations.

7. REFERENCES

- Ackerman, S. A., E. W. Eloranta, C. J. Grund, R. O. Knuteson, H. E. Revercomb, W. L. Smith and D. P. Wylie, 1993: University of Wisconsin Remote Sensing Pilot Experiment. Bull. A.M.S., **74**, 1041-1049.
- Grund, C. J. and E. W. Eloranta, 1991, University of Wisconsin high spectral resolution lidar., Optical Eng., **30**, 6-12.

- Hahn, C. J., C. S. Warren, J. London, R. M. Chervin and R. Jenne, 1982: Atlas of simultaneous occurrence of different cloud types over the oceans., NCAR Tech. Note NCAR TN-201+STR, National Center for Atmospheric Research, Boulder, CO, 212 pp.
- Krasnopolsky, V. M., and L. C. Breaker, 1994: The problem of AVHRR image navigation revisited., Int. J. Remote Sensing, **15**, 979-1008.
- Liou, K. N., An introduction to atmospheric radiation., Academic Press, Orlando, FL, 392 pp.
- Menzel, W. P., D. P. Wylie, and K. I. Strabala, 1992: Seasonal and diurnal changes in cirrus clouds as seen in four years of observations with the VAS., J. Appl. Meteor., **31**, 370-385.
- Minnis, P., D. F. Young, K. Sassen, J. M. Alvarez and C. J. Grund: 1990: The 27-28 October 1986 FIRE IFO Cirrus Case Study: Cirrus parameter relationships derived from satellite and lidar data., Mon. Wea. Rev., **118**, 2402-2425.
- Paltridge, G. W., 1980: Cloud-radiation feedback to climate., Quart. J. R. Met. Soc., **106**, 895-899.
- Piironen, P. and E. W. Eloranta, 1994: Demonstration of high-spectral-resolution lidar based on an iodine absorption filter., Optics Letters, **19**, 234-236.
- Platt, C. M. R., 1979: Remote sounding of high clouds: I. Calculation of visible and infrared optical properties from lidar and radiometer measurements., J. of Appl. Meteor., **18**, 1130-1143.
- Platt, C. M. R., and G. L. Stephens, 1980: The interpretation of remotely sensed high cloud emittances., J.A.S., **37**, 2314-2321.
- Platt, C. M. R., J. C. Scott, and C. Dille, 1987: Remote sounding of high clouds. Part VI: Optical properties of midlatitude and tropical cirrus., J.A.S., **44**, 729-747.
- Rossow, W. B., and R. A. Schiffer, 1991: ISCCP cloud data products., Bull. Am. Meteor. Soc., **72**, 1-20.
- Schiffer, R. A., and W. B. Rossow, 1983: The International Cloud Climatology Project (ISCCP): The first project of the World Climate Research Programme., Bull. Am. Meteor. Soc., **64**, 779-784.
- Stephens, G. L., S. C. Tsay, P. W. Stackhouse, and P. J. Flatau, 1990: The relevance of the microphysical and radiative properties of cirrus clouds to climate and climatic feedback., J. Atm. Sci., **47**, 1742-1753.
- Stephens, G. L., 1994: Remote sensing of the lower atmosphere., Oxford University Press, New York, NY, 523 pp.
- Tselioudis, G., W. B. Rossow and D. Rind, 1992: Global Patterns of cloud optical thickness variation with temperature., J. of Climate., **5**, 1484-1497.
- Weare, B. C., 1992: Variations in Nimbus-7 cloud estimates. Part I: Zonal averages., J. Climate, **5**, 1496-1505.
- Wielicki, B. A., and J. A. Coakley, 1981: Cloud retrieval using infrared sounder data: Error analysis., J. Appl. Meteor., **20**, 157-169.

Woodbury, G. E., and M. P. McCormick, 1983: Global distributions of cirrus clouds determined from SAGE data., Geophys. Res. Letters, **10**, 1180-1183.

Wylie, D. P. and W. P. Menzel, 1989: Two years of cloud cover statistics using VAS. J. Clim. Appl. Meteor., **2**, 380-392.

Wylie, D. P., W. P. Menzel, H. M. Woolf and K. I. Strabala, 1994: Four years of global cirrus cloud statistics using HIRS., J. Climate, in press.

8. Acknowledgments

The Authors thank Barry Hinton and Dan Forrest for their constructive comments. This research was funded by grant NAG1-553 from NASA and grant F19628-91-K-0007 from the U. S. Air Force.

TABLE 1: The dates and times of the satellite-lidar comparisons.

<u>Month/Date</u> <u>/Year</u>	<u>Time</u>	<u>Satellite</u>	Optical Depth		
			Visible (τ_{vis})	Infrared (τ_{ir})	
08/24/93	01:30 UTC	NOAA-12	0.52	0.44	Multiple layers with water
09/02/93	01:37	NOAA-12	0.20	0.05	Thin and variable
09/08/93	01:08	NOAA-12	2.10	1.02	Multiple layers with water
10/02/93	00:51	NOAA-12	2.25	1.30	Thick cirrus
10/12/93	00:36	NOAA-12	0.91	0.34	Thin
10/25/93	00:57	NOAA-12	0.06	0.03	Thin and variable
10/26/93	00:35	NOAA-12	0.50	0.28	Uniform thin layer
10/28/93	01:32	NOAA-12	1.50	0.74	One thick layer
11/11/93	01:31	NOAA-12	1.00	0.61	Two layers with water
02/04/94	00:06, 00:36, 01:06 and 01:36	GOES	0.10	0.16	One thick layer
02/15/94	01:06	GOES	0.08	0.07	Thin layer
02/17/94	01:06	GOES	0.04	0.08	Thin layer trace of water
03/04/94	01:06	GOES	0.08	0.11	Thin layer
03/08/94	01:09	NOAA-12	0.73	0.19	Two layers with water
03/17/94	01:09	GOES	0.07	0.14	Thin layer
03/26/94	00:06, 00:36, 01:06 and 01:36	GOES	1.32	0.70	Thick layer
04/07/94	00:22	NOAA-12	0.15	0.20	Thin layer
04/11/94	00:36	NOAA-12	0.76	0.34	Thick layer
04/15/94	00:49	NOAA-12	0.75	1.07	Two layers with water

LIST OF FIGURES

Figure 1: The physical thickness vs. the visible optical depth of semi-transparent clouds observed by the HSRL in 1993 and 1994.

Figure 2: Scatter plot of the visible and infrared optical depths measured by the combination of the HSRL lidar (visible optical depth at $0.53 \mu\text{m}$) and NOAA and GOES satellite data (infrared $10.8 \mu\text{m}$ window channel). The diagonal line is a ratio of 2.0 (visible/IR). Error bars are shown on each data point.

Figure 3: Time-height image of the backscatter cross section $\beta_a(r) \frac{P(\pi, r)}{4\pi}$ (see Eq. 2) from the HSRL (upper panel). The lower panel is the visible optical depth from the integral of extinction from 8.5 to 12 km altitude on 26 October 1993.

Figure 4: NOAA-12 1 km HRPT image from AVHRR Channel 4 ($10.8 \mu\text{m}$) from 26 October 1993. This image was remapped into an equal distant latitude-longitude projection. The location of the HSRL is indicated by the black dot.

Figure 5: Time-height image of the backscatter cross section $\beta_a(r) \frac{P(\pi, r)}{4\pi}$ (see Eq. 2) from the HSRL (upper panel). The lower panel is the visible optical depth from the integral of extinction from 4 to 10 km altitude on 11 November, 1993. The extremely white layers between 5 and 5.5 km were liquid water as determined from depolarization measurements (not shown).

Figure 6: NOAA-12 1 km HRPT image from AVHRR Channel 4 ($10.8 \mu\text{m}$) from 11 November 1993. This image was remapped into an equal distant latitude-longitude projection. The location of the HSRL is indicated by the black dot.

Figure 7: Time-height image of the backscatter cross section $\beta_a(r) \frac{P(\pi, r)}{4\pi}$ (see Eq. 2) from the HSRL (upper panel). The lower panel is the visible optical depth from the integral of extinction from 7 to 11 km altitude on 2 September, 1993.

Figure 8: NOAA-12 AVHRR Channel 4 infrared image from 2 September, 1993.

Figure 9: Time-height image of the backscatter cross section $\beta_a(r) \frac{P(\pi, r)}{4\pi}$ (see Eq. 2) from the HSRL (upper panel). The lower panel is the visible optical depth from the integral of extinction from 3.5 to 11 km altitude on 15 April, 1994.

Figure 10: NOAA-12 AVHRR Channel 4 infrared image from 15 April, 1994.

Figure 11: The cross wind (top panel) and along the wind (bottom panel) images of range corrected backscatter from the Volume Imaging Lidar for 19:50 UT (13:50 CST) on 1 December 1989 at Madison, WI.

Figure 12: Same as Fig. 11 for 20:07 UT (15:07 CST) on 1 December 1989.

Figure 13: Error or difference in vertically integrated backscatter for an area vs. a line average, plotted as a function of separation distance between the locations of the area and line averaged volumes for the period of 19:30 to 20:30 UT, 1 December, 1989.

Figure 14: Same as Fig. 12 for the period, 20:30 to 21:30 UT, 1 December, 1989.

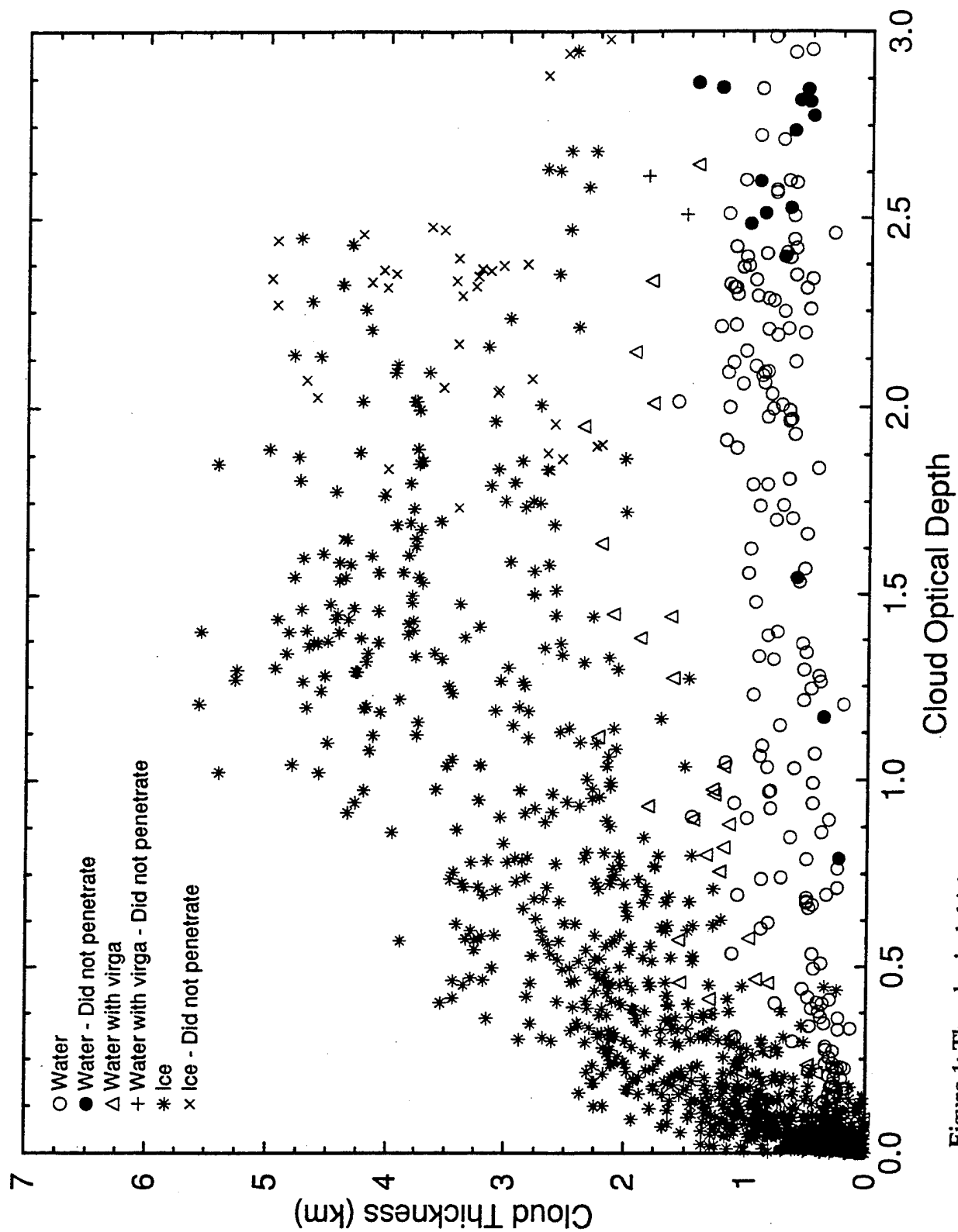


Figure 1: The physical thickness vs. the visible optical depth of semi-transparent clouds observed by the HSRL in 1993 and 1994.

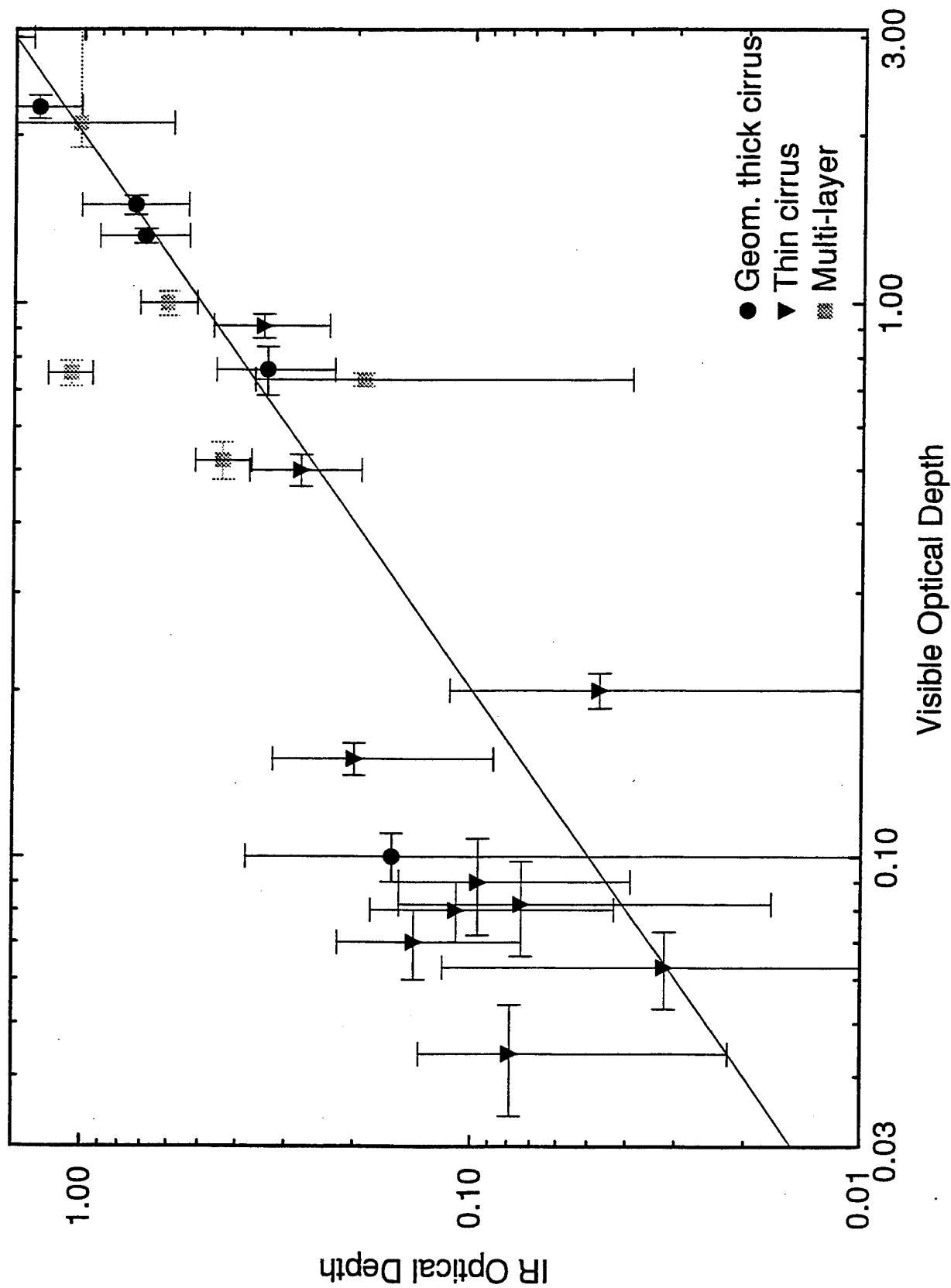


Figure 2: Scatter plot of the visible and infrared optical depths measured by the combination of the HSRL lidar (visible optical depth at $0.53 \mu\text{m}$) and NOAA and GOES satellite data (infrared $10.8 \mu\text{m}$ window channel). The diagonal line is a ratio of 2.0 (visible/IR). Error bars are shown on each data point.

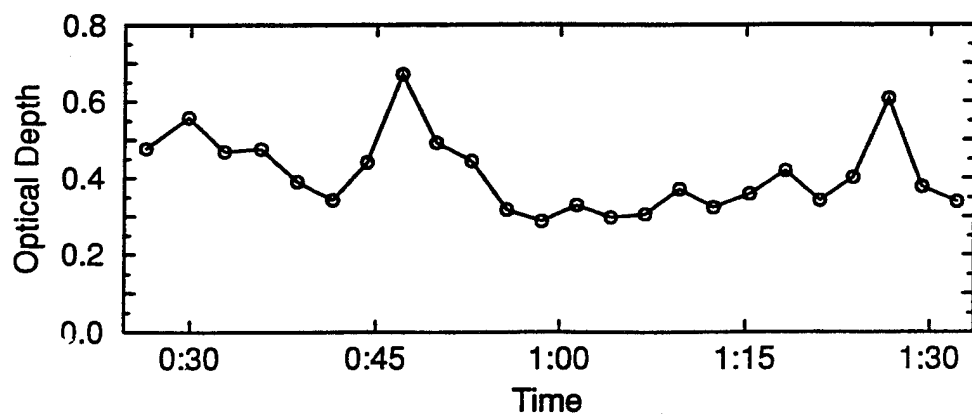
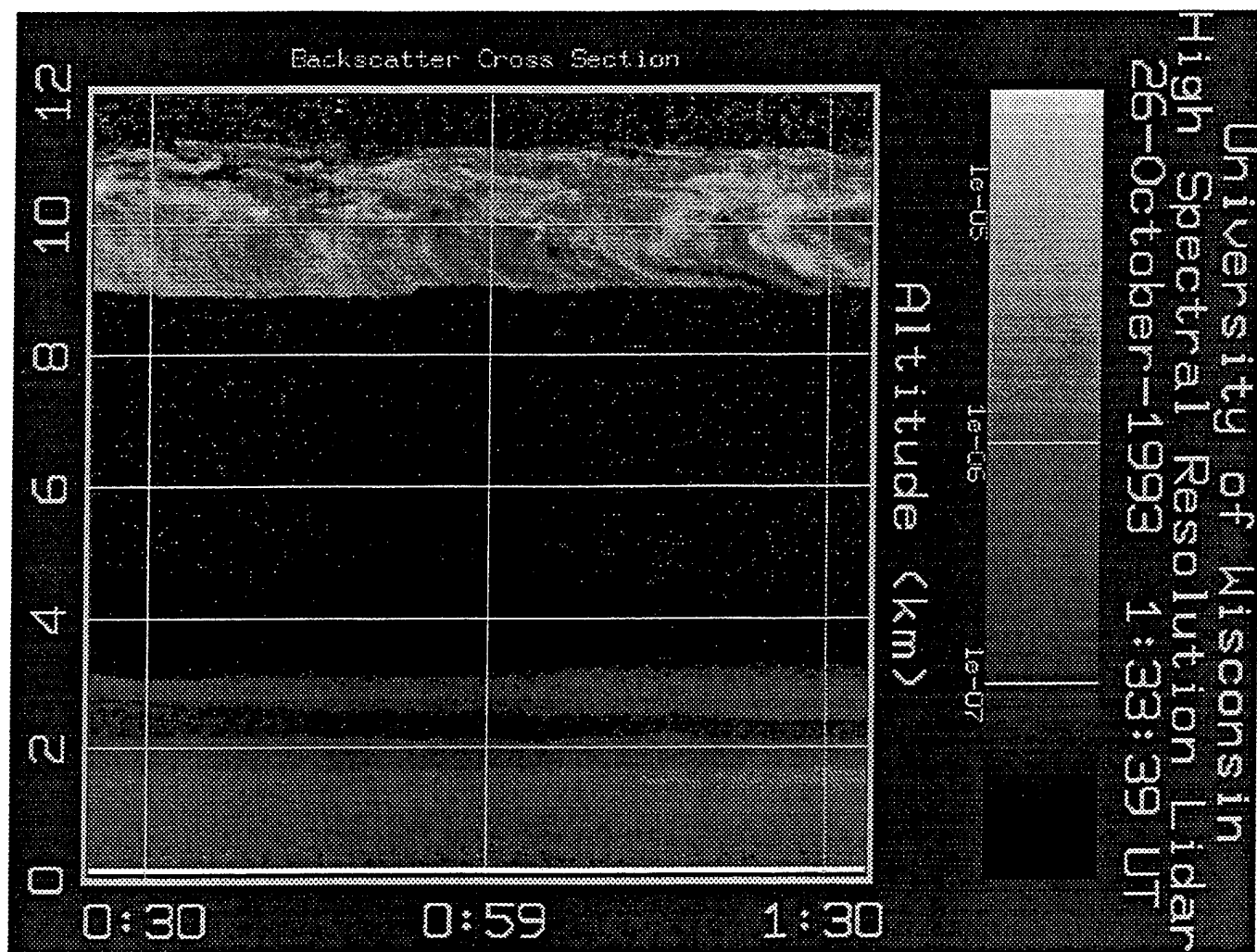


Figure 3: Time-height image of the backscatter cross section $\beta_a(r) \frac{P(\pi, r)}{4\pi}$ (see Eq. 2) from the HSRL (upper panel). The lower panel is the visible optical depth from the integral of extinction from 8.5 to 12 km altitude on 26 October 1993.

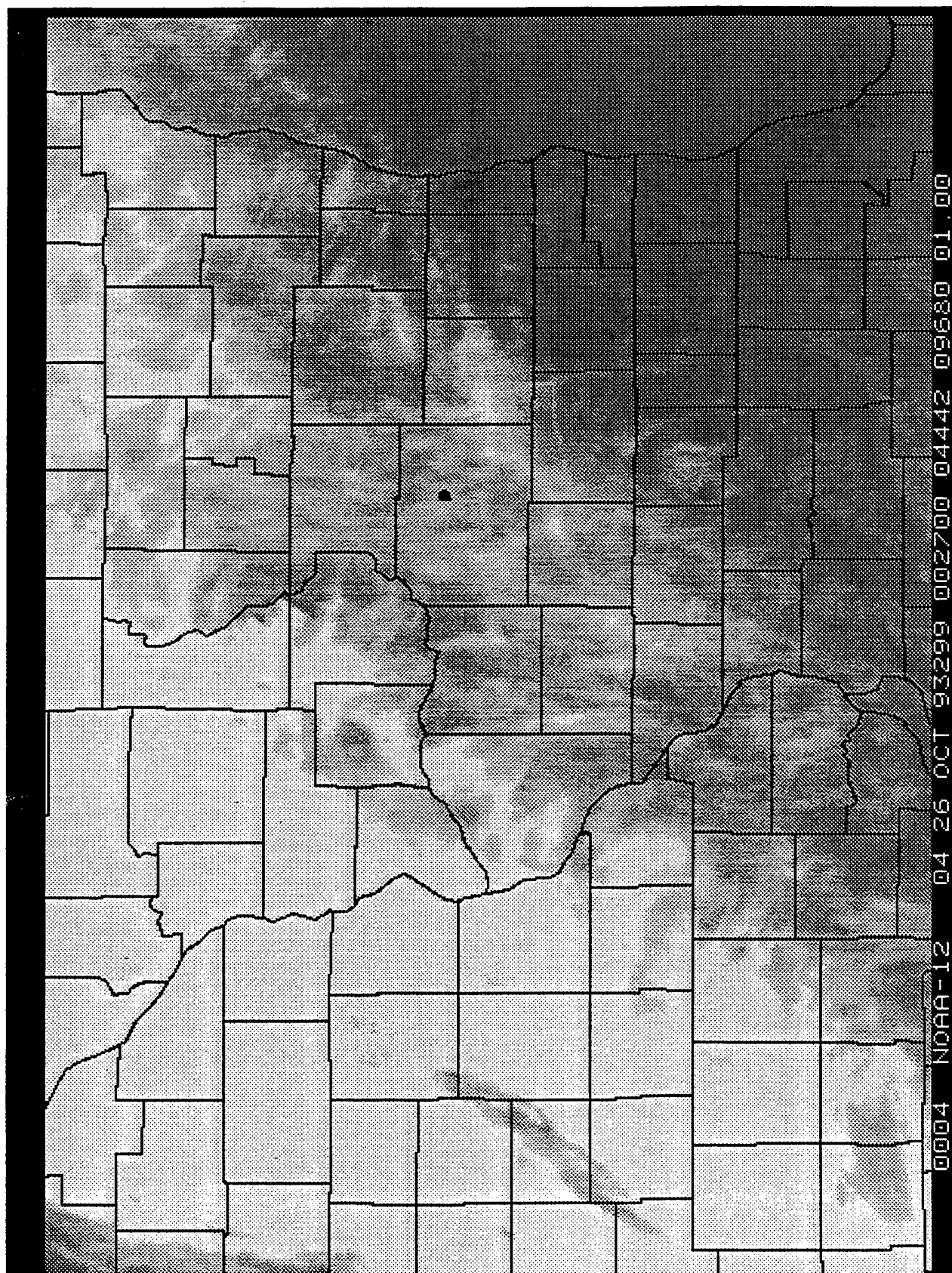


Figure 4: NOAA 12 1 km HRPT image from AVHRR Channel 4 ($10.8 \mu\text{m}$) from 26 October 1993. This image was remapped into an equal distant latitude-longitude projection. The location of the HSRL is indicated by the black dot.

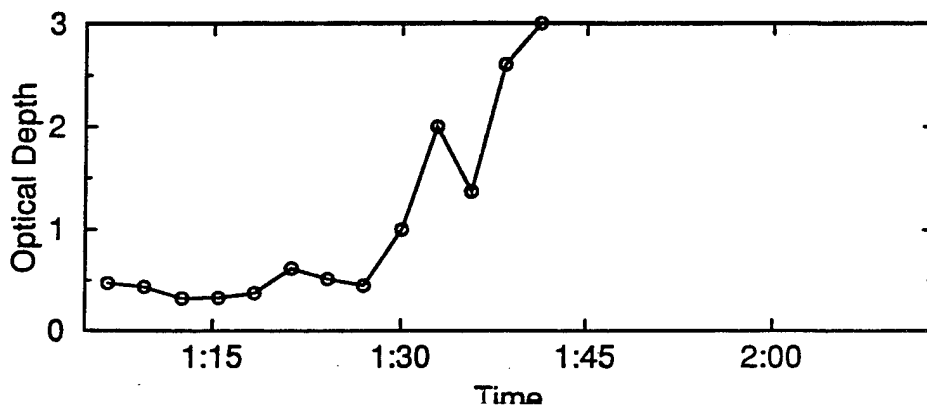
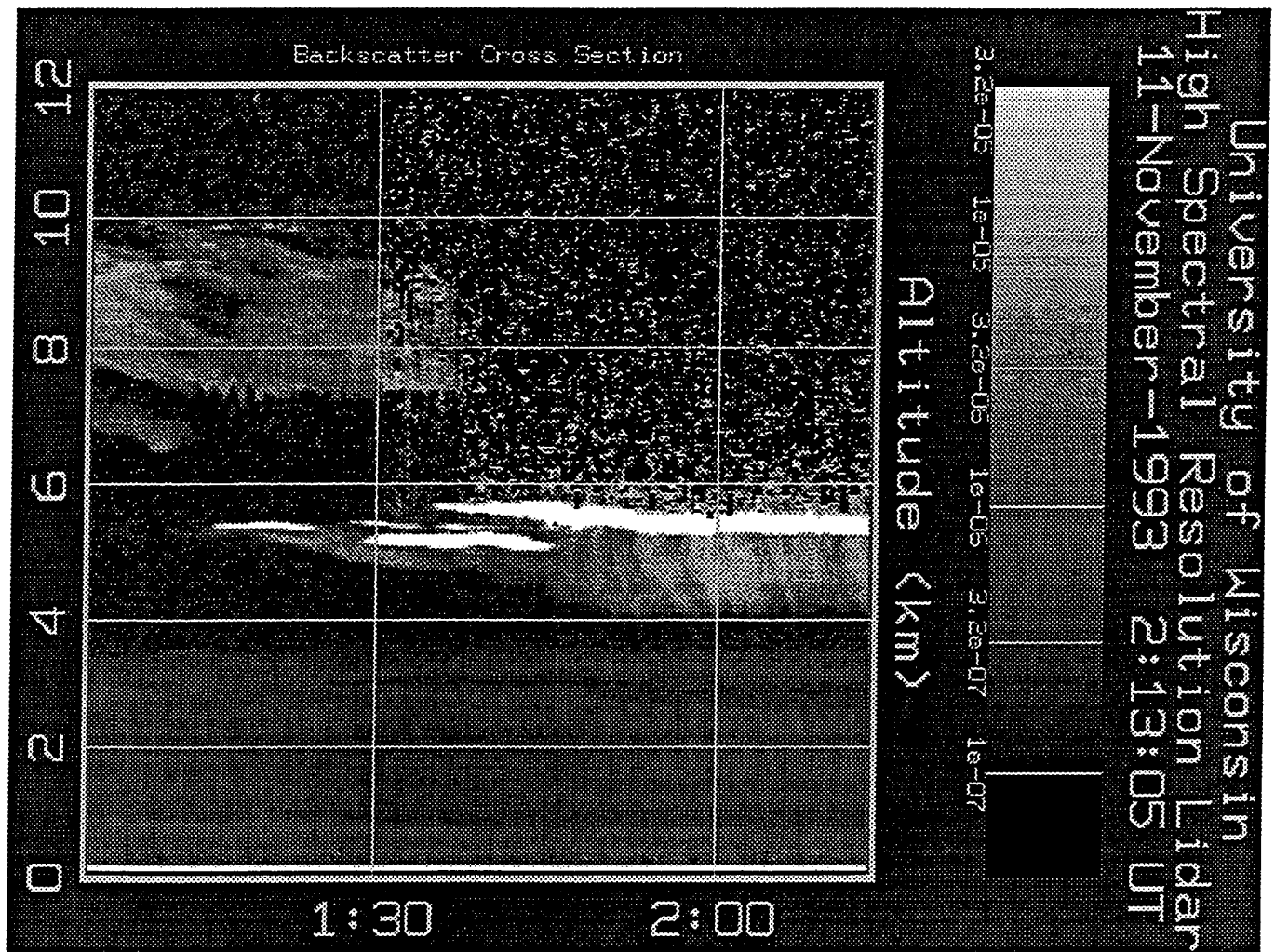


Figure 5: Time-height image of the backscatter cross section $\beta_a(r) \frac{P(\pi, r)}{4\pi}$ (see Eq. 2)

from the HSRL (upper panel). The lower panel is the visible optical depth from the integral of extinction from 4 to 10 km altitude on 11 November, 1993. The extremely white layers between 5 and 5.5 km were liquid water as determined from depolarization measurements (not shown).

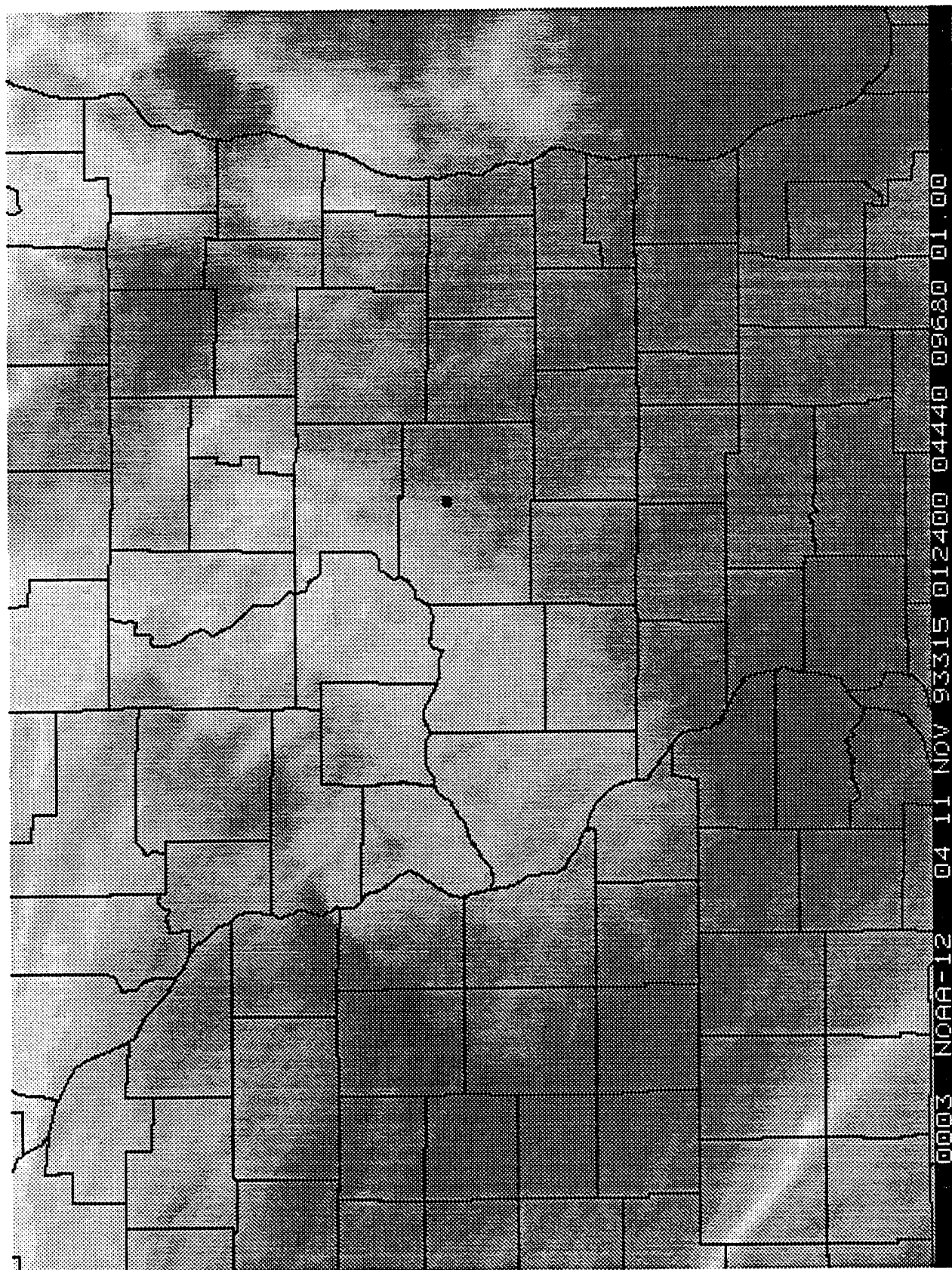


Figure 6: NOAA 12 1 km HRPT image from AVHRR Channel 4 ($10.8 \mu\text{m}$) from 11 November 1993. This image was remapped into an equal distant latitude-longitude projection. The location of the HSRL is indicated by the black dot.

University of Wisconsin
High Spectral Resolution Lidar
2-September-1993 3:04:17 UT

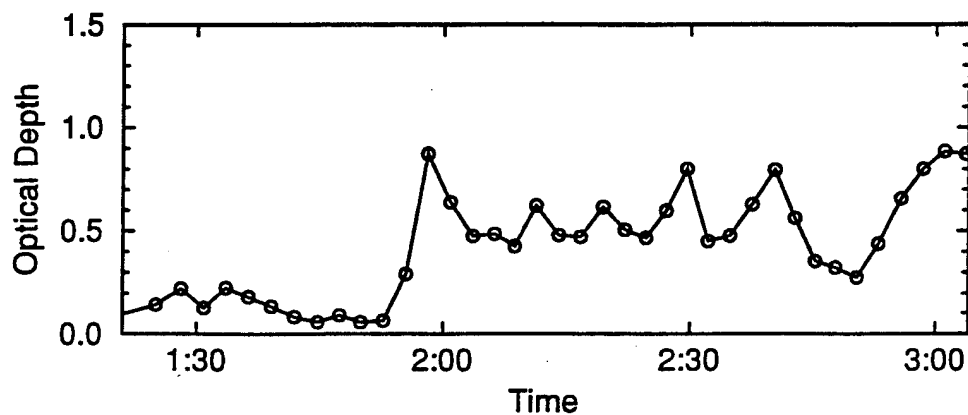
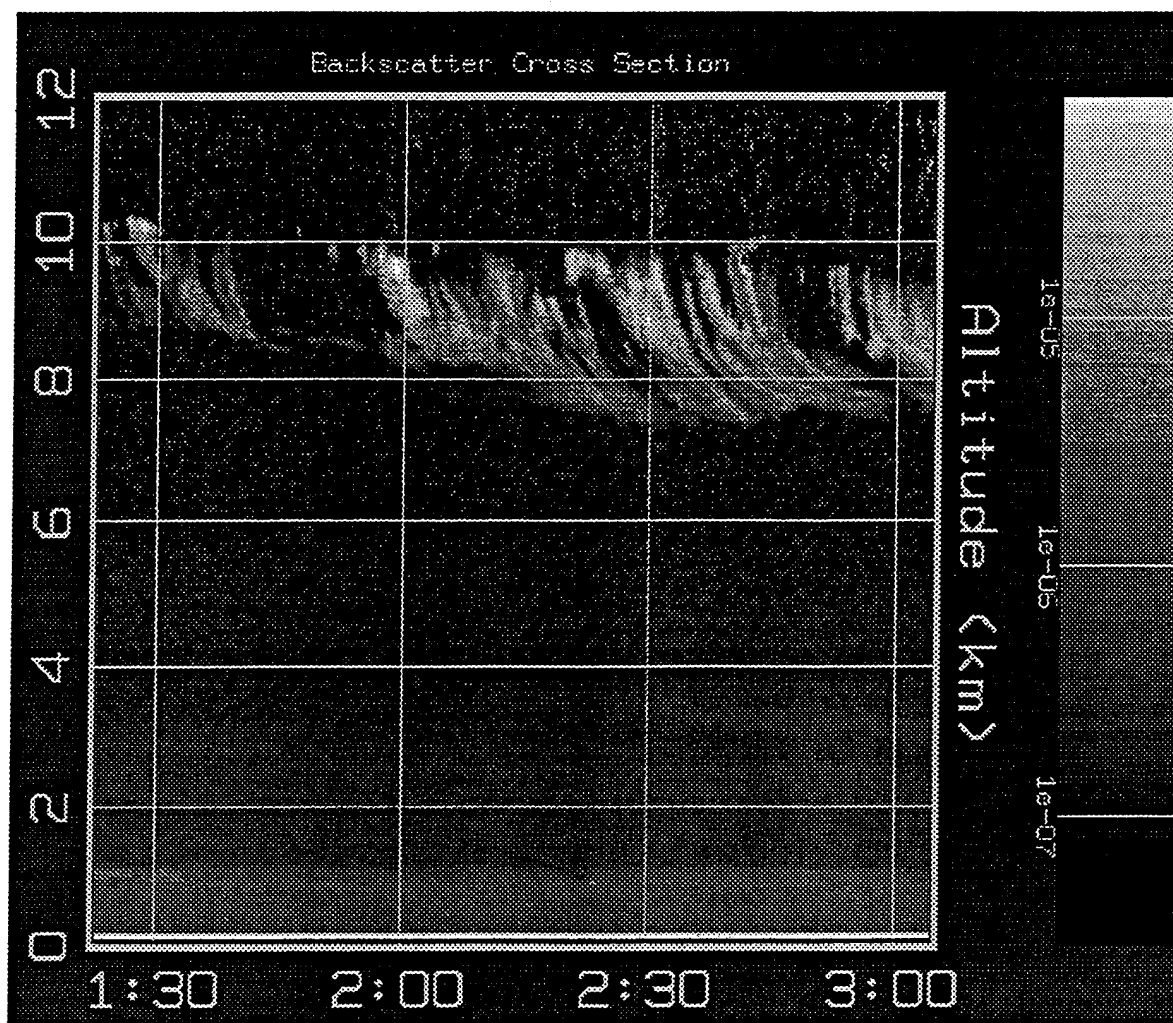


Figure 7: Time-height image of the backscatter cross section $\beta_a(r) \frac{P(\pi, r)}{4\pi}$ (see Eq. 2) from the HSRL (upper panel). The lower panel is the visible optical depth from the integral of extinction from 7 to 11 km altitude on 2 September, 1993.

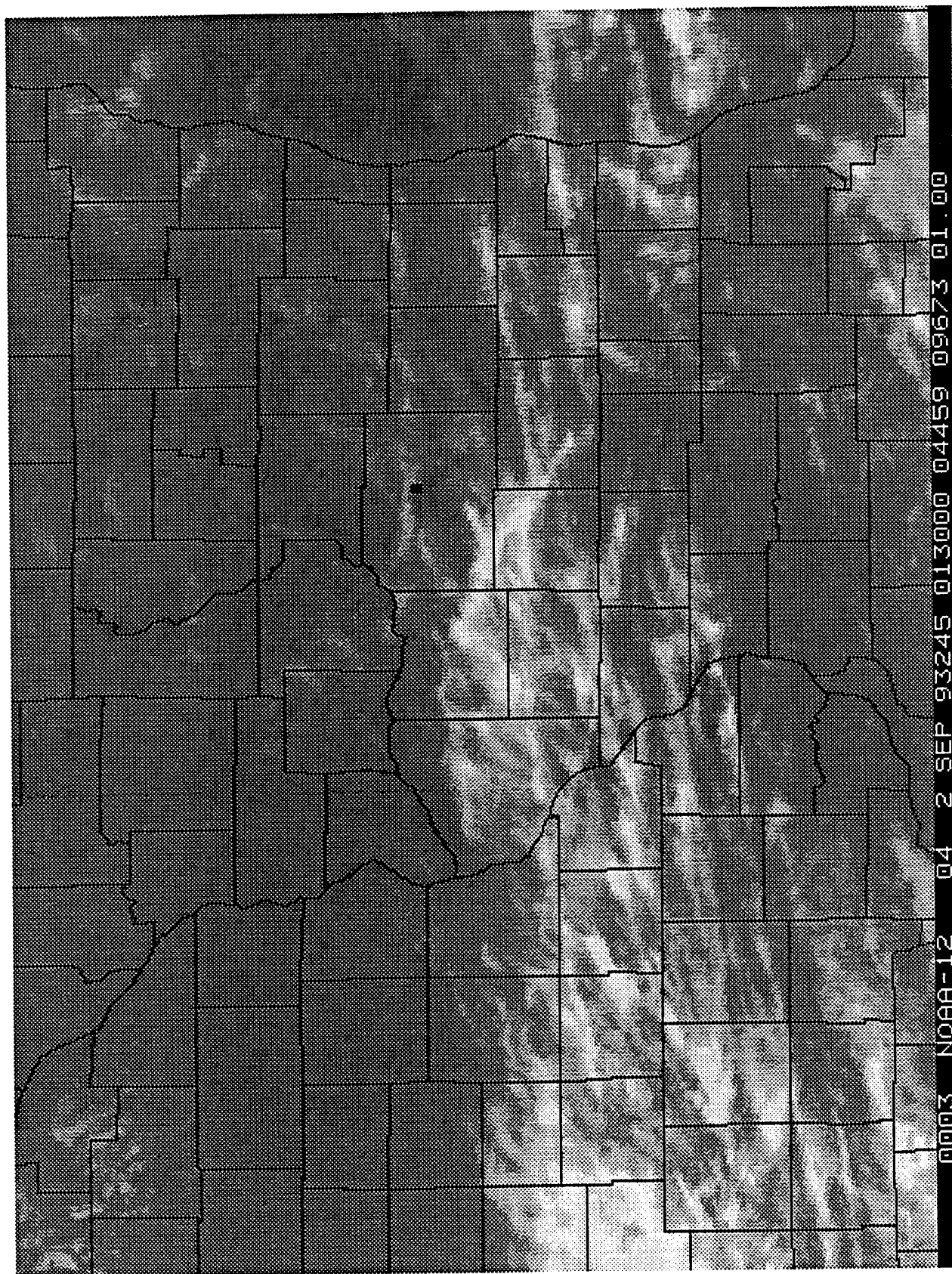


Figure 8: NOAA 12 AVHRR Channel 4 infrared image from 2 September, 1993.

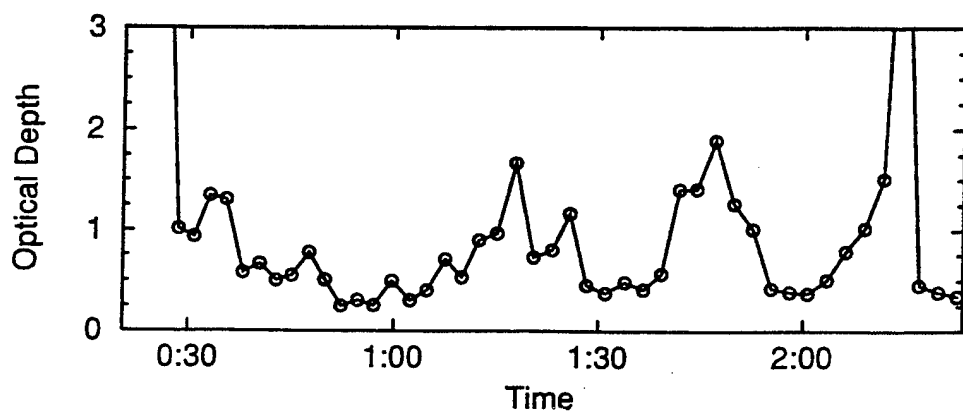
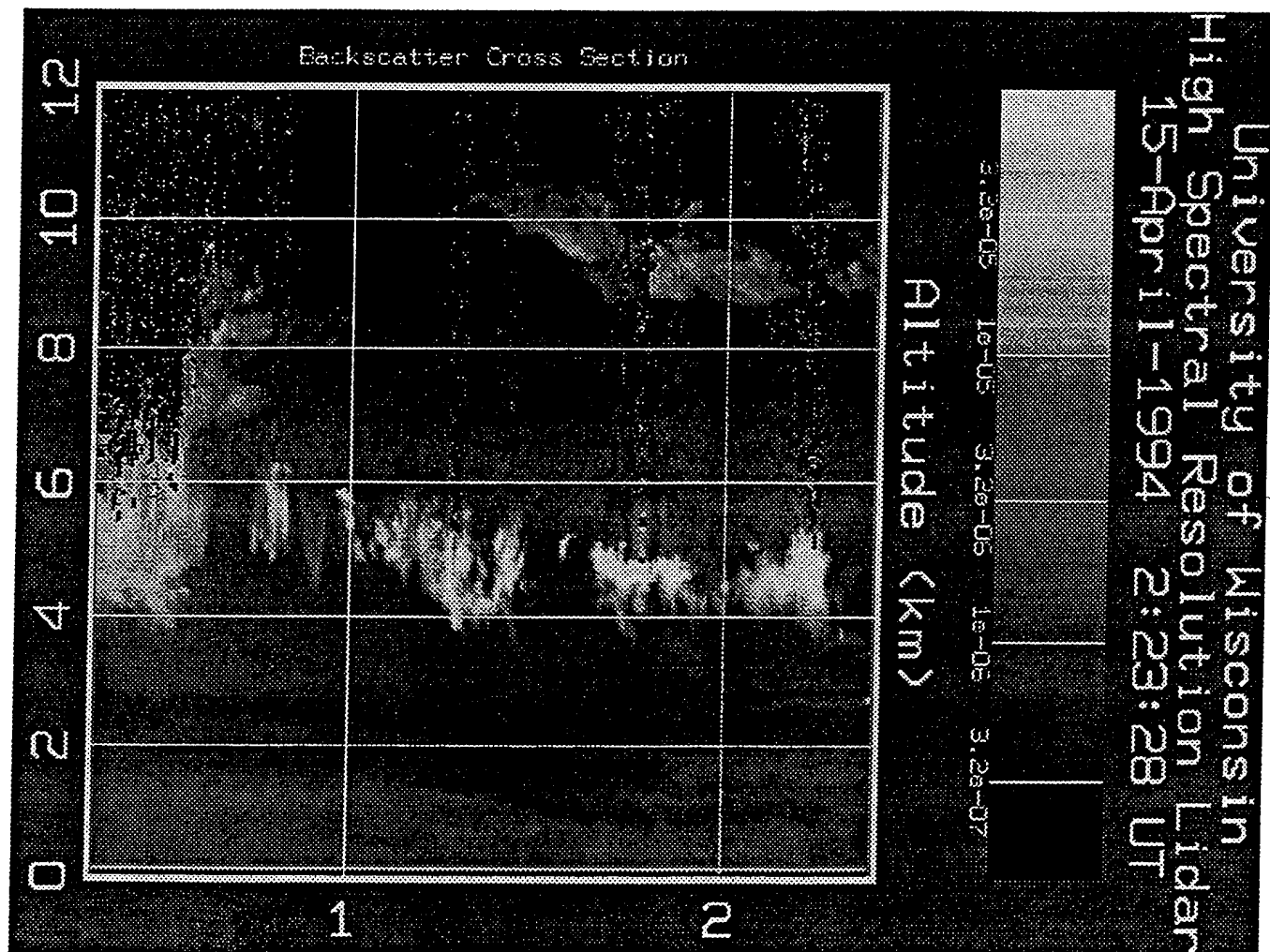


Figure 9: Time-height image of the backscatter cross section $\beta_a(r) \frac{P(\pi, r)}{4\pi}$ (see Eq. 2) from the HSRL (upper panel). The lower panel is the visible optical depth from the integral of extinction from 3.5 to 11 km altitude on 15 April, 1994.

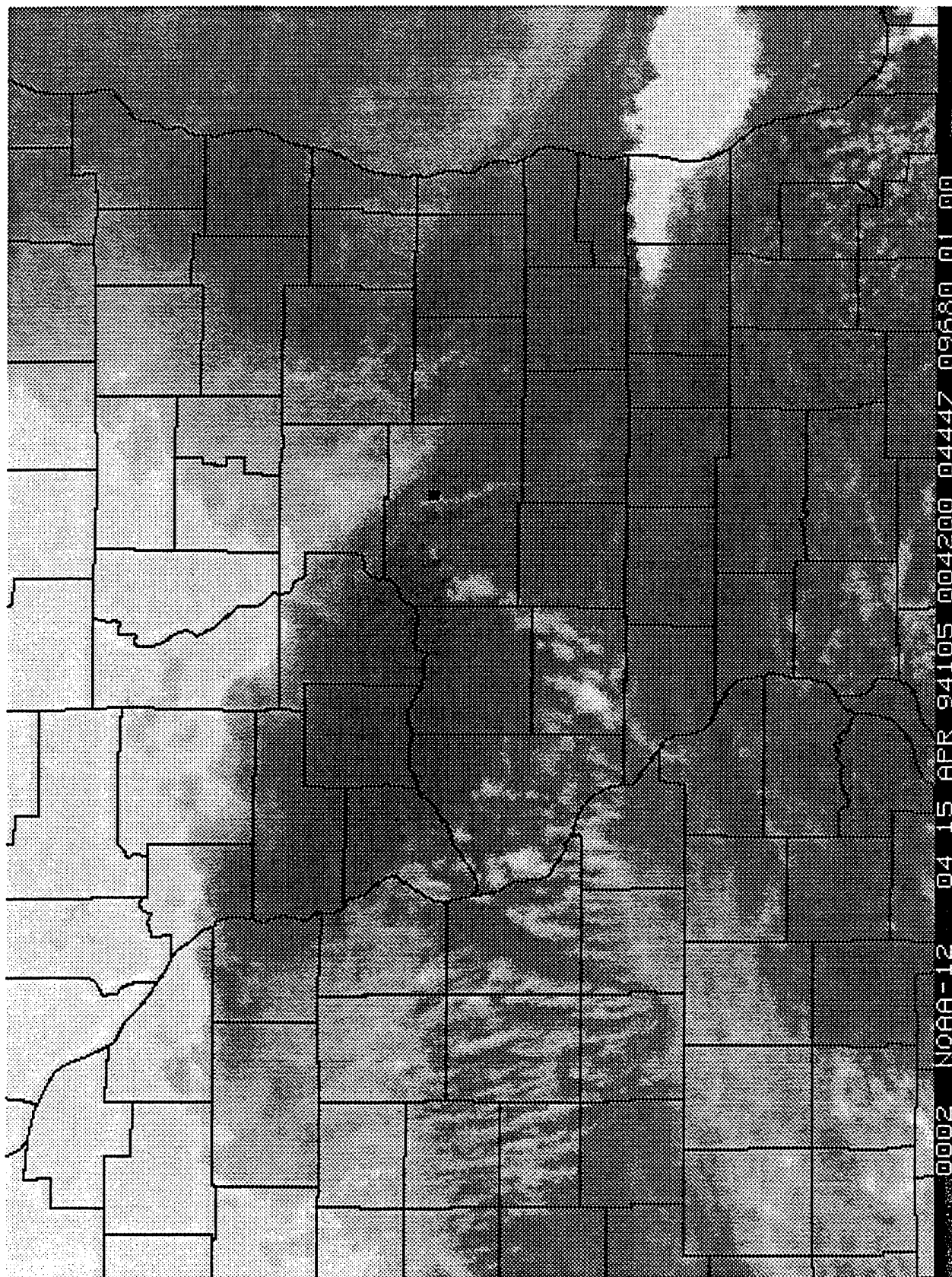


Figure 10: NOAA 12 AVHRR Channel 4 infrared image from 15 April, 1994.

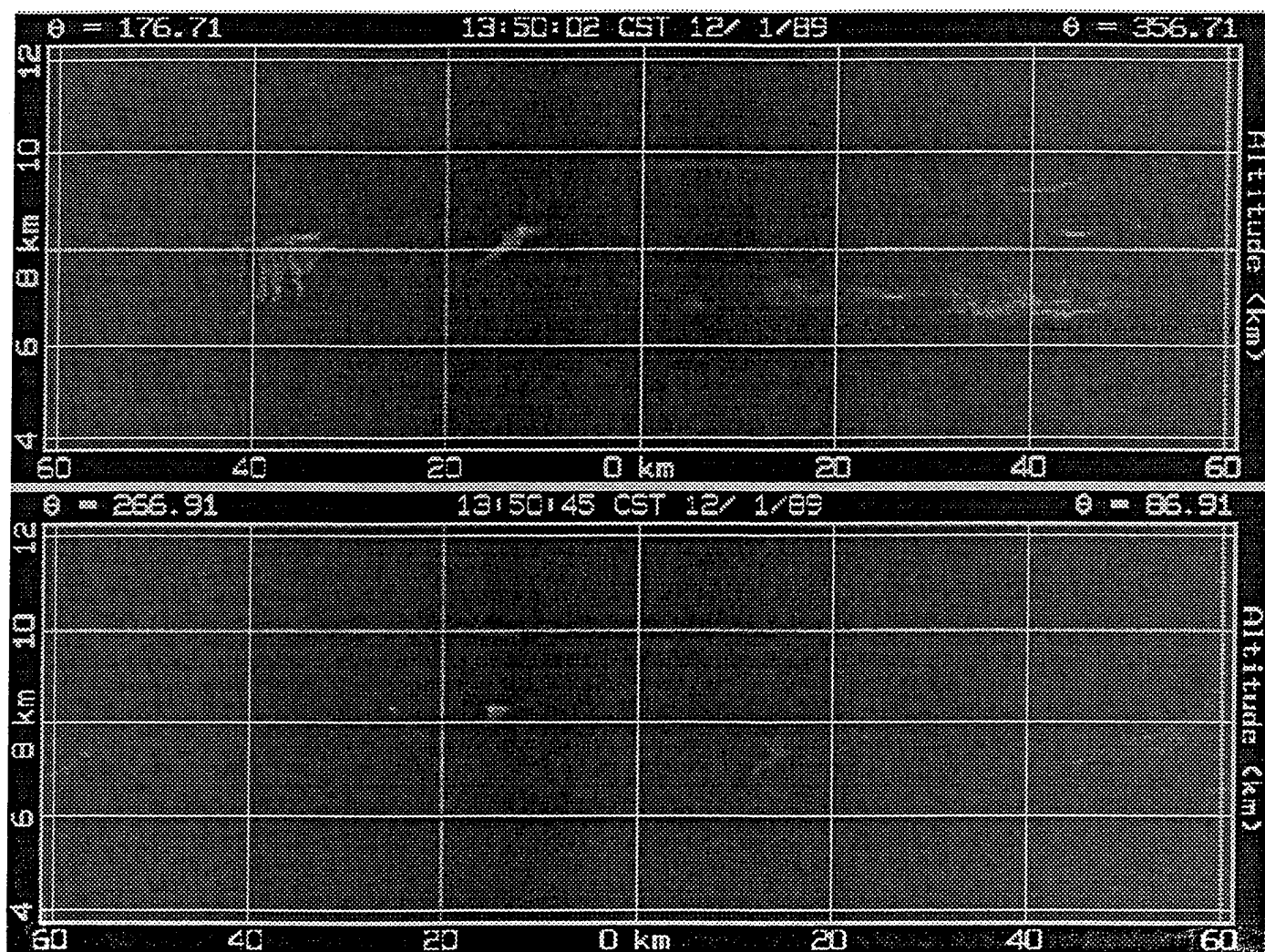


Figure 11: The cross wind (top panel) and along the wind (bottom panel) images of range corrected backscatter from the Volume Imaging Lidar for 19:50 UT (13:50 CST) on 1 December 1989 at Madison, WI.

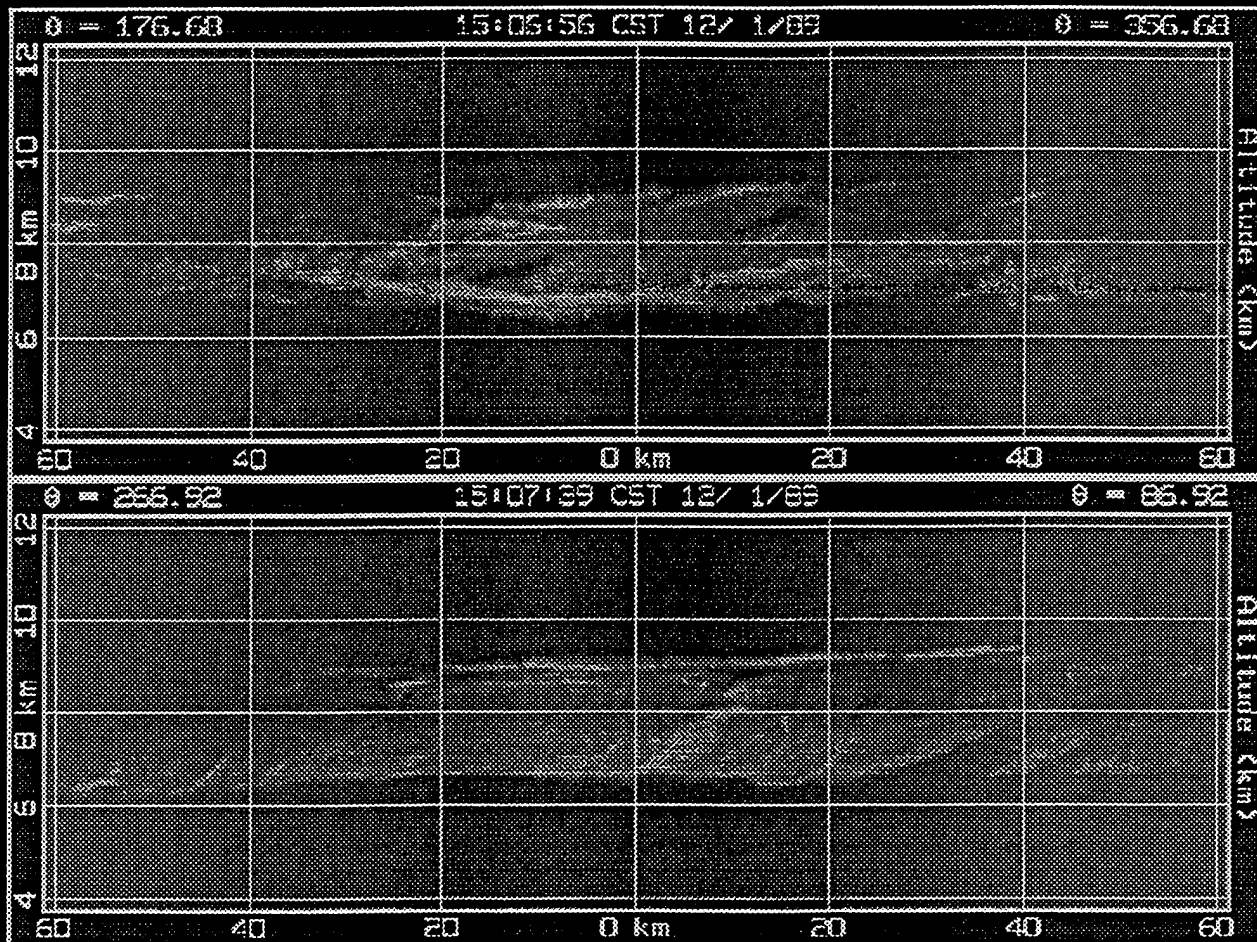


Figure 12: Same as Fig. 11 for 20:07 UT (15:07 CST) on 1 December 1989.

Line Average vs. Area Average

December 1, 1989 (19:29 - 20:25 GMT)

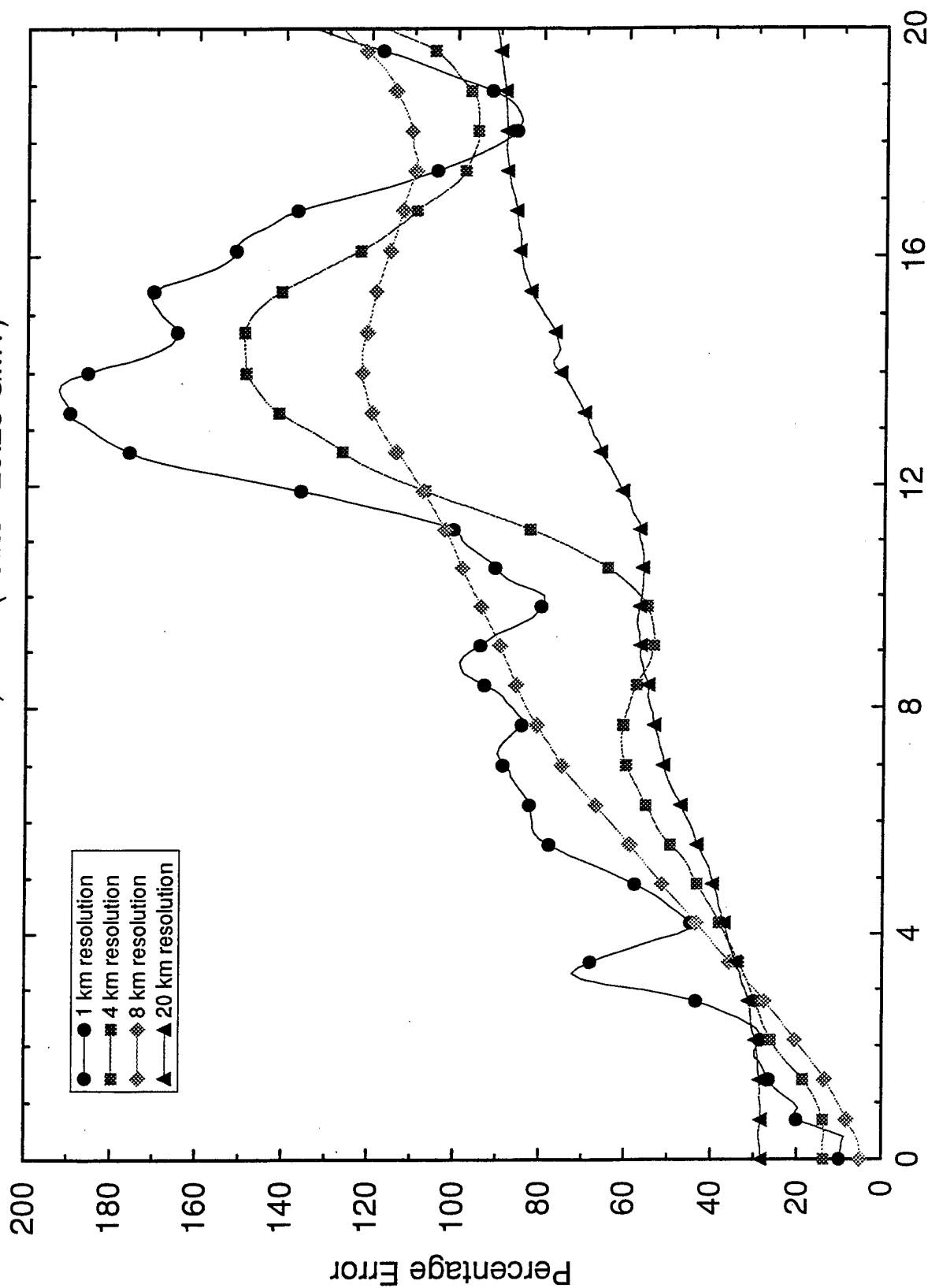


Figure 13: Error or difference in vertically integrated backscatter for an area vs. a line average, plotted as a function of separation distance between the locations of the area and line averaged volumes for the period of 19:30 to 20:30 UT, 1 December, 1989.

Line Average vs. Area Average

December 1, 1989 (20:25 - 21:20 GMT)

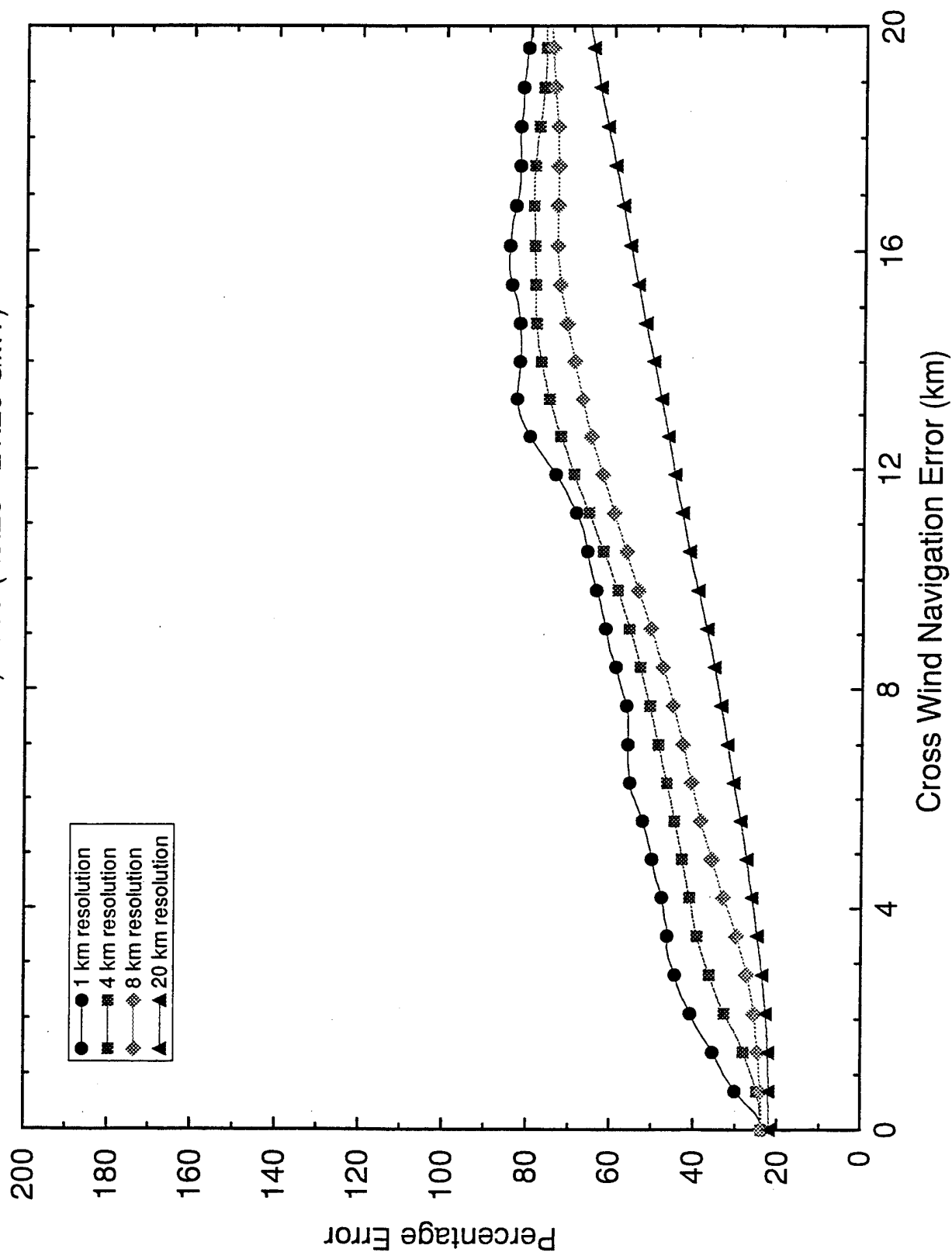


Figure 14: Same as Fig. 13 for the period, 20:30 to 21:30 UT, 1 December, 1989.